JM PAPERS

Lift force on a spherical droplet in a viscous linear shear flow

Pengyu Shi[1,2,†], Éric Climent[1] and Dominique Legendre[1,†]

[1]Université de Toulouse, INPT, UPS, IMFT (Institut de Mécanique des Fluides de Toulouse), F-31400 Toulouse, France

[2]Institute of Fluid Dynamics, Helmholtz-Zentrum Dresden – Rossendorf, 01328 Dresden, Germany

We study numerically the flow around a spherical droplet set fixed in a linear shear flow with moderate shear rates ($Sr \leq 0.5$, Sr being the ratio between the velocity difference across the drop and the relative velocity) over a wide range of external Reynolds numbers ($0.1 < Re \leq 250$, Re based on the slip velocity and the viscosity of the external fluid) and drop-to-fluid viscosity ratios ($0.01 \leq \mu^* \leq 100$). The flow structure, the vorticity field and their intrinsic connection with the lift force are analysed. Specifically, the results on lift force are compared with the low-Re solution derived for droplets of arbitrary μ^*, as well as prior data at finite Re available in both the clean-bubble limit ($\mu^* \to 0$) and the solid-sphere limit ($\mu^* \to \infty$). Notably, at $Re = O(100)$, the lift force exhibits a non-monotonic transition from $\mu^* \to 0$ to $\mu^* \to \infty$, peaking at $\mu^* \approx 1$. This behaviour is related to an internal three-dimensional flow bifurcation also occurring under uniform-flow conditions, which makes the flow to evolve from axisymmetric to biplanar symmetric. This flow bifurcation occurs at low-but-finite μ^* when the internal Reynolds number (Re^i, based on the viscosity of the internal fluid) exceeds approximately 300. In the presence of shear, the corresponding imperfect bifurcation enhances the extensional rate of the flow in the wake. Consequently, the streamwise vortices generated behind the droplet can be more intense compared with those behind a clean bubble. Given the close relation between the lift and these vortices, a droplet with $Re = O(100)$ and $\mu^* \approx 1$ typically experiences a greater lift force than that in the inviscid limit.

Key words: drops, multiphase flow

† Email addresses for correspondence: p.shi@hzdr.de, dominique.legendre@imft.fr

1. Introduction

Predicting the motion of droplets in dispersed two-phase flows is a key problem in fluid mechanics that has a bearing on a wide range of applications from epidemiology, microfluidic biotechnologies to chemical or petroleum engineering. Droplets maintain a spherical shape when interfacial tension forces or viscous dissipation significantly outweigh inertial and buoyancy effects, a condition commonly met by small-sized fluid particles. Under steady state, the motion of a spherical droplet is governed by two distinct hydrodynamic forces: drag (usually counterbalanced by the joint effects of the net gravity force and hydrostatic pressure), which reduces the relative motion; and lift, which is perpendicular to the relative motion and causes cross-stream droplet migration. While much experimental and numerical studies have been devoted to the drag, knowledge about lift, despite its nearly equal importance in predicting droplet motion in complex flows, remains limited (Magnaudet 2003; Di Carlo 2009; Elghobashi 2019; Mathai, Lohse & Sun 2020; Bourouiba 2021). Note, however, that the importance of lift cannot be fully inferred by comparing its magnitude with drag, as the two forces are, by definition, always perpendicular, and comparing their magnitudes does not reveal their relative importance in the dynamics they influence (Colin, Fabre & Kamp 2012). A typical situation where lift plays a key role while its magnitude remains vanishingly small with respect to drag is the inertial migration of particles/droplets in a shear flow in the low (slip)-Reynolds-number limit. This is the case, for instance, in the experiment of Segré & Silberberg (1962*a*,*b*), where neutrally buoyant spheres in laminar pipe flow were found to accumulate at a radial equilibrium position away from the centre. This equilibrium position results from a competition between the inertial lift contributed from shear, slip and the wall (Asmolov 1999; Matas, Jeffrey & Guazzelli 2009).

Due to its fore–aft symmetry, a spherical droplet experiences a lift force only when finite inertial effects are present (Bretherton 1962; Saffman 1965; Legendre & Magnaudet 1997). This inertia is characterized by the (external) Reynolds number $Re = u_{rel}(2R)/v$, where u_{rel} represents the relative velocity, R the radius of the droplet and v the kinematic viscosity of the external fluid. At low Re, the lift force arises from the vortical mechanism (Legendre & Magnaudet 1997; Magnaudet, Takagi & Legendre 2003): the shear in the ambient flow causes weak asymmetric advection of the vorticity from the droplet surface, causing a correction force which has a non-zero component in the transverse direction, i.e. a lift force. A key feature revealed by this mechanism is that the lift force is proportional to ω_s^2, the square of the maximum vorticity generated at the droplet surface. Specifically, the matching of the internal and external tangential velocity and viscous stress at the interface yields $\omega_s R/u_{rel} \propto (2+3\mu^*)/(2+2\mu^*)$, where μ^* is the (dynamic) viscosity ratio of the internal and external fluids. Therefore, to leading order, the lift force on a droplet in the clean-bubble limit (i.e. $\mu^* \to 0$) differs from that in the solid-sphere limit (i.e. $\mu^* \to \infty$) by only a factor of $(2/3)^2$.

The lift force generated by the vortical mechanism decreases as Re increases. Then, if μ^* is small, a second, inviscid mechanism takes over. This mechanism involves the tilting of the ambient vorticity by the sphere, which leads to the generation of a pair of counterrotating vortices in the wake of the droplet. This is the classical Lighthill mechanism (Lighthill 1956; Auton 1987) (hereafter referred to as the '*L*' mechanism), which corresponds to a lift force proportional to the ambient vorticity and pointing in the same direction as that predicted by the low-Re vortical mechanism. In addition to the '*L*' mechanism, a so-called '*S*' mechanism (Adoua, Legendre & Magnaudet 2009) also comes into play at moderate-to-high Re. Similar to the '*L*' mechanism, it also generates two counter-rotating streamwise vortices in the wake. However, these are formed due to the tilting of the surface-generated vorticity ω_s by the velocity gradient of the ambient

1000 A88-2

flow, with orientations opposite to those induced by the '*L*' mechanism (refer to (3.2) in § 3.3.2 for more details on the distinction between the two mechanisms). The '*S*' mechanism, being intrinsically related to ω_s, has a negligible effect in the clean-bubble limit, as $\omega_s(\mu^* \to 0)$ never exceeds $3u_{rel}/R$ (Batchelor 1967, p. 366). Conversely, in the solid-sphere limit and at high enough *Re*, it likely overwhelms the '*L*' mechanism, as $\omega_s(\mu^* \to \infty)$ scales with $Re^{1/2}$ (Magnaudet, Rivero & Fabre 1995). The significance of this '*S*' mechanism for droplets with finite viscosity ratios, corresponding to liquid droplets in an ambient immiscible liquid, remains an open question.

Previous studies on fluid spheres with finite μ^* moving at finite *Re* have primarily focused on specific scenarios like a water droplet in air (i.e. $\mu^* \approx 50$) and an air bubble in water (i.e. $\mu^* \approx 0.02$) (Bothe, Schmidtke & Warnecke 2006; Fukuta, Takagi & Matsumoto 2008; Sugioka & Komori 2009; Suh & Lee 2013; Albert *et al.* 2015). Owing to the substantial viscosity difference between water and air, the lift on a spherical water droplet (respectively, a spherical air bubble) is found to be almost identical to that of a solid sphere (respectively, a clean bubble). Specifically, in the limit $\mu^* \to \infty$, the lift force switches from positive (corresponding to the vortical mechanism) to negative (corresponding to the '*S*' mechanism) beyond $Re \approx 55$ (Kurose & Komori 1999; Bagchi & Balachandar 2002; Shi & Rzehak 2019). In contrast, such a reversal is absent in the $\mu^* \to 0$ limit, as the inviscid mechanism takes over and remains dominant whatever the Reynolds number (Legendre & Magnaudet 1998; Takagi & Matsumoto 1998, 2011).

Considering the various observations summarized above, three key questions emerge. (i) How is the transition of lift force from the clean-bubble limit to the solid-sphere one? (ii) How does the viscosity ratio influence lift reversal? (iii) At finite μ^*, are the two previously mentioned mechanisms still active? Namely, the '*L*' mechanism associated with inviscid tilting of the ambient vorticity and the '*S*' mechanism associated with the vorticity generated at the droplet surface; and if so, how do they interact? This work aims to address these questions by numerically solving the three-dimensional (3-D) flow around and inside a spherical droplet set fixed in an uniform shear flow over a wide range of Reynolds numbers and drop-to-fluid viscosity ratios. We then use the results obtained for the flow field to elucidate the different mechanisms involved in generating the lift force.

The paper is organized as follows. In § 2, we formulate the problem, specify the considered range of parameters and outline the numerical approach, which closely follows the methodology used by Rachih (2019) and Legendre *et al.* (2019), supplemented with preliminary tests to validate its reliability. Section 3 offers a comprehensive discussion of the results obtained in this work. Specifically, § 3.1 focuses on the original evolution observed for the drag and lift forces over the considered range of Reynolds numbers, which imply a non-monotonic evolution of both drag and lift with the viscosity ratio at $Re = O(100)$. Section 3.2 outlines the identification of an internal 3-D flow bifurcation occurring at moderate-to-high Reynolds numbers, which leads to a non-monotonic variation in both the drag and lift forces in this regime. Section 3.3 is dedicated to illustrating the physical mechanisms revealed from the flow field that contribute to the lift force at high Reynolds numbers. The influence of the shear rate is discussed in § 3.4. Empirical fits reproducing the observed variations in specific regimes are established in § 3.5. Concluding remarks, as well as issues remaining open from this work, are presented in § 4.

2. Statement of the problem and outline of the numerical approach

We consider a spherical droplet with radius *R*, density ρ^i and dynamic viscosity μ^i, fixed at the origin of a Cartesian frame of reference $(\boldsymbol{e}_x, \boldsymbol{e}_y, \boldsymbol{e}_z)$, as illustrated in figure 1.
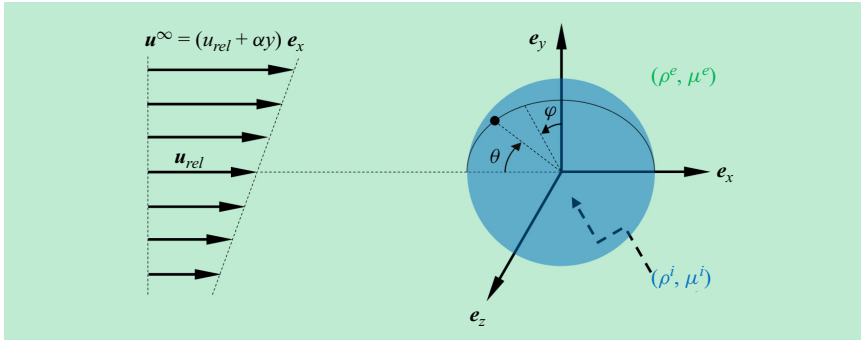
Figure 1. Sketch of the problem. Here, u^∞ denotes the flow in the undisturbed far field with a shear rate α; ρ^e and μ^e (respectively, ρ^i and μ^i) denote the density and dynamic viscosity of the external (respectively, internal) fluid; and θ and φ represent the polar and azimuthal angles, respectively.

This droplet is immersed in a Newtonian fluid characterized by density ρ^e and dynamic viscosity μ^e. In its undisturbed state, the external flow is a linear shear along e_x, described by

$$u^\infty = (u_{rel} + \alpha y)e_x, \tag{2.1}$$

where u_{rel} represents the norm of the slip velocity u_{rel}, i.e. $u_{rel} = ||u_{rel}||$. The entire flow field is governed by the incompressible Navier–Stokes equations,

$$\nabla \cdot u^k = 0, \quad \rho^k \left(\frac{\partial u^k}{\partial t} + u^k \cdot \nabla u^k \right) = -\nabla p^k + \nabla \cdot \tau^k, \tag{2.2a,b}$$

where $\tau^k = \mu^k(\nabla u^k + {}^T\nabla u^k)$ is the viscous part of the stress tensor $\Sigma^k = -p^k I + \tau^k$, u^k and p^k denote the disturbed velocity and the pressure, respectively, with $k = i$ (likewise, $k = e$) denotes the fluid inside (outside) the droplet. Right at the surface of the droplet, the normal velocity must vanish, owing to the non-penetration condition, while the tangential velocity and shear stress are continuous. These yield the following boundary conditions at the droplet surface $r = R$:

$$u^i \cdot n = u^e \cdot n = 0, \quad n \times u^i = n \times u^e, \quad n \times (\tau^i \cdot n) = n \times (\tau^e \cdot n), \tag{2.3a–c}$$

where $r = (x^2 + y^2 + z^2)^{1/2}$ is the distance to the centre of the droplet and n is the outward unit normal to the droplet surface.

In the region far from the droplet, we assume that the disturbance induced by the droplet vanishes, namely

$$u^e = u^\infty \quad \text{for } r = \infty. \tag{2.4}$$

The steady-state solution of the problem is characterized by four key parameters: the viscous ratio $\mu^* = \mu^i/\mu^e$, the external Reynolds number Re, the dimensionless shear rate Sr and the Reynolds number ratio Re^*. The last three are defined as

$$Re = \frac{\rho^e u_{rel}(2R)}{\mu^e}, \quad Sr = \frac{\alpha(2R)}{u_{rel}}, \quad Re^* = \frac{Re^i}{Re} = \frac{\rho^*}{\mu^*}, \tag{2.5a–c}$$

where $\rho^* = \rho^i/\rho^e$ denotes the drop-to-fluid density ratio and Re^i the Reynolds number based on the kinematic viscosity of the internal fluid. Unless otherwise stated, we fix $Sr = 0.2$ and $Re^* = 5$ by default, but vary μ^* and Re within the ranges of $[0.01, 100]$

and (0.1, 250], respectively. In practice, $Sr = 0.2$ corresponds, for example, to a 1.1 mm diameter *n*-pentane droplet rising at $16.4\,\mathrm{cm\,s^{-1}}$ in water with a shear of $40\,\mathrm{s^{-1}}$, an order of magnitude typical of turbulent shear layers. To address the influence of the shear rate, cases with smaller ($Sr = 0.02$) and larger ($Sr = 0.5$) shear rates under selected conditions are considered as well.

In most practical situations, rising or settling droplets do not remain spherical at high Reynolds numbers. Rather, they transform into oblate spheroids, characterized by an aspect ratio, χ, which is the length ratio of the major-to-minor axis. The value of χ largely depends on the Weber number, $We = \rho^e u_{rel}^2 (2R)/\gamma$, where γ represents the surface tension. For instance, an *n*-pentane droplet rising in water remains nearly spherical ($\chi < 1.1$) for Reynolds numbers up to approximately 400 (Godé 2023), corresponding to $We \approx 2$. For a droplet of arbitrary ρ^* and μ^* moving at $Re = O(100)$, previous direct numerical simulation and experimental results (Dandy & Leal 1989; Loth 2008) have indicated that χ at a given We depends only weakly on ρ^*, but increases with decreasing viscosity ratio μ^*. In pure water under standard conditions, bubbles with $\chi = 1.1$ have an equivalent radius of approximately 0.52 mm and a rise velocity of $u_{rel} \approx 0.27\,\mathrm{m\,s^{-1}}$ (Duineveld 1995), corresponding to a Weber number of approximately 1 and a rise Reynolds number of approximately 280. This is why, in the present work, we set the upper limit of the Reynolds number at 250. If one regards a droplet with $\chi < 1.1$ as nearly spherical, the results obtained with spherical droplets may be considered valid up to a Weber number of approximately 1, regardless of ρ^* and μ^*. Since we only consider moderate shear rates ($Sr = 0.2$ for most cases), shear-induced deformations are smaller than those due to slip (Adoua *et al.* 2009), and the above conclusion extends to droplets rising in a linear shear flow.

The considered range of μ^* allows us to examine the transition of the hydrodynamic force from the clean-bubble limit ($\mu^* \to 0$) to the solid-sphere limit ($\mu^* \to \infty$). Similarly, the selected Re range helps investigate the hydrodynamic force from the Stokes-flow regime ($Re \to 0$), pertinent in inertial microfluidics, to a moderately inertial yet stationary regime ($Re = O(100)$ such that no vortex shedding takes place), relevant in applications like spray drying (Michaelides 2006), inkjet printing (Lohse 2022) and airtanker firefighting (Legendre 2024). Although the internal Reynolds number Re^i (and thus Re^*) does not influence the quasi-steady hydrodynamic force in the Stokes-flow regime (Magnaudet *et al.* 2003), it appears to significantly affect the force in the moderately inertial regime, especially when the wake of a droplet subjected to a uniform flow becomes asymmetric (Edelmann, Le Clercq & Noll 2017; Rachih *et al.* 2020). To explore this, we also vary Re^* within the range of [0.2, 10] at $Re = 200$.

We are particularly interested in obtaining the hydrodynamic force acting on the droplet. This force can be decomposed into a drag component F_D, parallel to $\boldsymbol{u}_{rel}$ (and hence $\boldsymbol{e}_x$) and a lift or transverse component, F_L, parallel to $\boldsymbol{e}_y$. They are defined as

$$F_D = \boldsymbol{e}_x \cdot \int_{\Gamma} \boldsymbol{\Sigma}^e \cdot \boldsymbol{n}\,\mathrm{d}\Gamma, \quad F_L = \boldsymbol{e}_y \cdot \int_{\Gamma} \boldsymbol{\Sigma}^e \cdot \boldsymbol{n}\,\mathrm{d}\Gamma, \qquad (2.6a,b)$$

where Γ denotes the droplet surface. The results for these two forces are expressed in terms of the dimensionless drag and lift coefficients, C_D and C_L, calculated by normalizing the forces with $\pi R^2 \rho^e u_{rel}^2/2$. Additionally, we denote the drag and lift coefficients in the clean-bubble and solid-sphere limits as C_D^B, C_L^B and C_D^S, C_L^S, respectively.

Note that the imposed boundary conditions (continuity of velocity and tangential stress) at the interface allow the internal and external fluids to move freely. Only the spherical shape is imposed and a circulating interface is possible. Note also that the lift coefficient

defined above differs from that used in previous studies investigating the lift force on bubbles (e.g. Auton 1987; Legendre & Magnaudet 1998; Tomiyama *et al.* 2002). In these studies, the lift force is normalized by $\rho^e V_s \boldsymbol{u}_{rel} \times \boldsymbol{\omega}^\infty$, where $\boldsymbol{\omega}^\infty = \boldsymbol{\nabla} \times \boldsymbol{u}^\infty$ represents the vorticity of the local undisturbed flow and V_s is the volume of the droplet. In the inviscid limit, the lift coefficient according to this previous normalization is 0.5, whereas it is $2Sr/3$ with the normalization used in this work. The reason for adopting a different normalization of the lift force concerns the possible presence of a non-zero lift force in an irrotational flow where $\omega^\infty = 0$. Specifically, for a uniform flow past a solid sphere, the axial symmetry in the wake is known to break down at a critical Reynolds number $Re^{SS} \approx 212.6$ through a stationary (external) bifurcation (Fabre, Tchoufag & Magnaudet 2012), leading to a non-zero lift force at larger Reynolds numbers whose orientation is selected by some initial disturbance. This force grows proportionally to the square root of $Re - Re^{SS}$, as shown by Citro *et al.* (2016) and Shi & Rzehak (2019), particularly when Re increases up to 250 (the maximum Re considered in this work). Consequently, following the previous normalization method (i.e. normalized by $\rho^e V_s \boldsymbol{u}_{rel} \times \boldsymbol{\omega}^\infty$), the lift coefficient would reach infinity when the flow with $\omega^\infty = 0$ becomes non-axisymmetric. No such singularity appears if C_L is calculated by normalizing the lift force with $\pi R^2 \rho^e u_{rel}^2/2$. A summary of previously obtained expressions for C_L^S and C_L^B, following the normalization in this work, is given in Appendix B.

The simulations were performed using the JADIM code developed at IMFT. This code has been applied previously to simulate the lift on bubbles and solid spheres (Legendre & Magnaudet 1998; Adoua *et al.* 2009; Shi 2021), and extended for calculating the 3-D flows around and inside spherical droplets (Legendre *et al.* 2019; Rachih *et al.* 2020; Godé *et al.* 2023). The Navier–Stokes equations are solved using velocity-pressure variables in orthogonal curvilinear coordinates, discretized on a staggered grid. Spatial integration is achieved through a finite-volume method with second-order accuracy. The advection and viscous terms are evaluated using second-order centred schemes, while time advancement is managed with a second-order Runge–Kutta–Crank–Nicolson algorithm. Incompressibility is ensured at the end of each time step by solving, for each fluid, a Poisson equation for an auxiliary potential.

The computational domain is cylindrical, aligned along $\boldsymbol{e}_x$ and divided into two blocks by the droplet surface. To mitigate the confinement effects at low Reynolds numbers, we set the radius (R_y^∞) and height (R_x^∞) of the cylinder to $100R$ for $Re < 10$. For $10 \leq Re \leq 250$, R_y^∞ is reduced to $50R$ to leverage the faster decay of the disturbance flow at higher Re, while R_x^∞ is increased to $200R$ to ensure adequate dissipation of the far wake within the computational domain. The domain is discretized using an axisymmetric mesh, detailed by Rachih *et al.* (2020, figure 1). Inside the droplet, we employ a polar mesh with N_θ nodes in the polar direction (spanning from $\theta = 0$ to π; refer to figure 1 for the definition of θ) and N_r nodes radially. The external domain, in the same (θ, r)-plane, is discretized using an orthogonal mesh based on constant streamlines $\eta = $ const. and equipotential lines $\zeta = $ const. of the potential flow around a circle moving along $\boldsymbol{e}_x$. The entire grid in the (θ, r)-plane is then rotated around the x axis by $\varphi = 2\pi$, with N_φ nodes along φ. The grid inside the droplet comprises $N_\theta \times N_r \times N_\varphi$ nodes, while the external grid has $(2N_\zeta + N_\theta) \times N_\eta \times N_\varphi$ nodes. Following Legendre *et al.* (2019), Rachih *et al.* (2020) and Shi (2021), we set $N_\theta = 80$, $N_r = 40$, $N_\varphi = 64$ and $N_\eta = 50$, regardless of Re. We increase N_ζ from 60 to 120 as Re exceeds 10 to better resolve the far wake downstream at moderate-to-high Re. The nodes are uniformly distributed along θ and φ, while a geometric progression is chosen along r, ζ and η, ensuring at least five nodes located within the internal and external boundary layers at the interface for Reynolds numbers up to 1000.

1000 A88-6

The numerical boundary conditions are outlined as follows. The velocity at the top and bottom surfaces of the cylinder ($x = \pm R_x^\infty$) and the cylindrical surface [$(x^2 + y^2)^{1/2} = R_y^\infty$] is assumed to match the undisturbed flow, as defined in (2.1). At the droplet interface, boundary conditions (2.3b,c) are implemented using a second-order finite-difference discretization (Legendre *et al.* 2019; Rachih *et al.* 2020). The artificial singularity introduced by the $\boldsymbol{e}_x$-symmetry axis is addressed using a specific condition detailed by Legendre & Magnaudet (1998). The computation initiates from an undisturbed external flow and a stagnant internal flow.

The reliability of our numerical approach is verified in Appendix A, where three additional tests are carried out. In the first test, simulations at extreme viscosity ratios μ^* are performed for $0.1 < Re \leq 250$. The hydrodynamic forces at $\mu^* = 0.01$ and 100 align well with existing correlations and data for spherical bubbles (Auton 1987; Mei, Klausner & Lawrence 1994; Legendre & Magnaudet 1997, 1998) and solid spheres (Schiller & Naumann 1933; Kurose & Komori 1999; Bagchi & Balachandar 2002; Shi & Rzehak 2019; Candelier *et al.* 2023). The second test examines a droplet with $\mu^* = 0.5$ at $Re = 200$ in a uniform flow ($Sr = 0$), varying Re^* from 0.2 to 10. This replicates the finding of Edelmann *et al.* (2017) that the flow around a droplet of $\mu^* = O(1)$ undergoes a bifurcation when Re^i exceeds approximately 300. Our results for the drag and separation angle (after the bifurcation sets in) agree well with those from Feng & Michaelides (2001, C_D prior to the onset of flow bifurcation) and Edelmann *et al.* (2017). The final test cross-checks our results at moderately high Re against those from Zhang (2023, private communication), in which simulations are carried out using the numerical code Basilisk (Popinet 2009, 2015). We focus on two cases with different viscosity ratios, one at $\mu^* = 0.2$ and the other at $\mu^* = 0.5$, while both correspond to $Re = 200$, $Re^* = 5$ and $Sr = 0.2$. The time histories of C_D and C_L from both codes show excellent agreement, further confirming the reliability of the numerical approach applied in this work.

3. Results and discussion

3.1. *Drag and lift forces*

Figure 2 shows the numerical results for the drag and lift coefficients at $Re = 0.2$. Clearly, both coefficients increase monotonically with increasing μ^*. This is consistent with the low-Re vortical mechanism (Legendre & Magnaudet 1997; Magnaudet *et al.* 2003), which suggests that the drag and lift increase with increasing surface vorticity (i.e. the vorticity generated on the external side of the droplet) and, hence, with increasing viscosity ratio μ^*. Specifically, the vortical mechanism indicates that, to leading order, the drag (respectively, lift) force in the solid-sphere limit at low-but-finite Re differs from that in the clean-bubble limit only by a prefactor of $3/2$ (respectively, $(3/2)^2$), $3/2$ being the ratio of the maximum surface vorticity, ω_s, in these two limits. This is confirmed by our numerical results, noting that C_D (respectively, C_L) at $\mu^* = 100$ is larger than that at $\mu^* = 0.01$ by a factor of 1.54 (respectively, 2.15).

Figure 3 presents the results for C_D and C_L within the low-to-moderate Reynolds number regime, $0.5 \leq Re \leq 20$. At a given Re, the computed C_D gradually increases with increasing μ^*, still aligning with the low-Re vortical mechanism. However, the behaviour of C_L differs. Specifically, C_L increases gradually with increasing μ^* only up to $Re \approx 2$. For $Re \geq 5$, it decreases as μ^* increases. This latter behaviour is not surprising. As Re increases, the ratio of the Oseen and Saffman lengths, $\varepsilon = (Sr/Re)^{1/2}$, a key parameter characterizing the magnitude of inertial lift (McLaughlin 1991), decreases as well. For $Re \gtrsim 5$, the lift generation is governed by the competition between the 'L' and 'S'
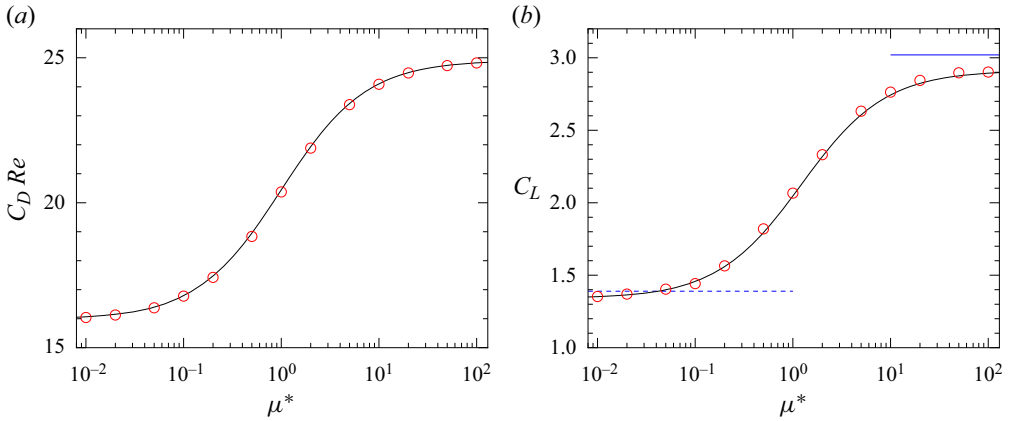
Figure 2. Results for C_D and C_L as a function of μ^* for $Re = 0.2$, $Re^* = 5$ and $Sr = 0.2$. Red circles, present numerical results. In panel (*a*), C_D is multiplied by Re for better readability; fitted line, (3.3*a*) with $m = 1$. In panel (*b*), fitted line, (3.3*b*); solid line, $C_L^{S(2)}$ according to (B3); dotted line, $C_L^{B(1)}$ according to (B4*b*).
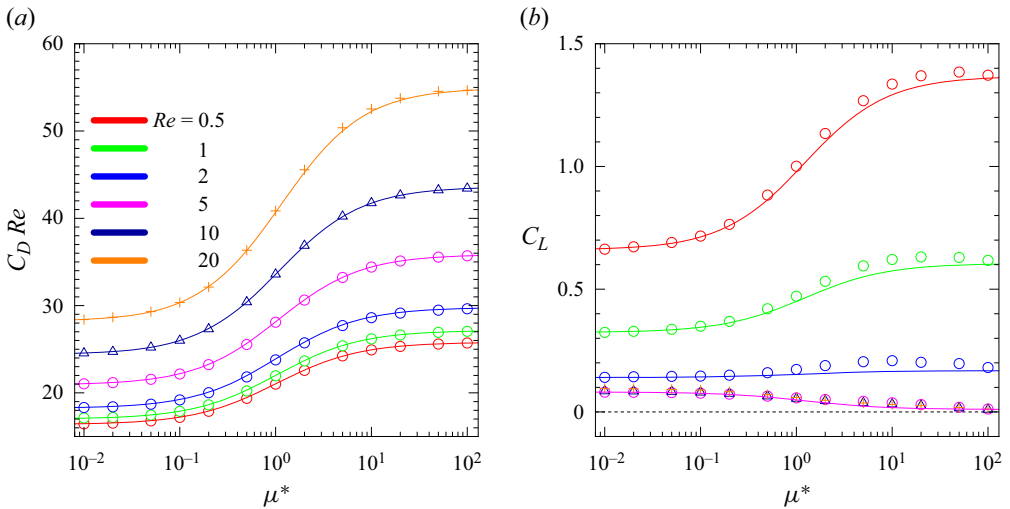

Figure 3. Similar to figure 2, but for $0.5 \leq Re \leq 20$, $Re^* = 5$ and $Sr = 0.2$. Different Re values are distinguished using the colours indicated in panel (*a*). Different types of symbols are used to represent data for $Re > 5$, providing a clearer distinction for the C_L results. In panel (*a*), solid lines correspond to predictions using (3.3*a*) with the expression for m from (3.4). In panel (*b*), solid lines denote predictions from (3.3*b*) and the horizontal thin dashed line represents $C_L = 0$.

mechanisms outlined in § 1. This competition will be elaborated on in more detail in § 3.3. Here, we briefly mention that the decrease in C_L with increasing μ^* for $Re \geq 5$ is closely related to the increase in the maximum surface vorticity ω_s. This increase enhances the '*S*' mechanism, resulting in an increasingly negative lift contribution (i.e. towards $-\boldsymbol{e}_y$) (Adoua *et al.* 2009; Hidman *et al.* 2022).

Figure 4 shows the drag and lift results at $Re = O(100)$. In contrast to the low-to-moderate Re regime, where C_D and C_L vary monotonically with increasing μ^*, these coefficients exhibit *non-monotonic* behaviour at low-but-finite μ^*. For instance, C_D at $Re = 250$ reaches a local maximum of 0.65 at $\mu^* = 2$, corresponding to 91 % of
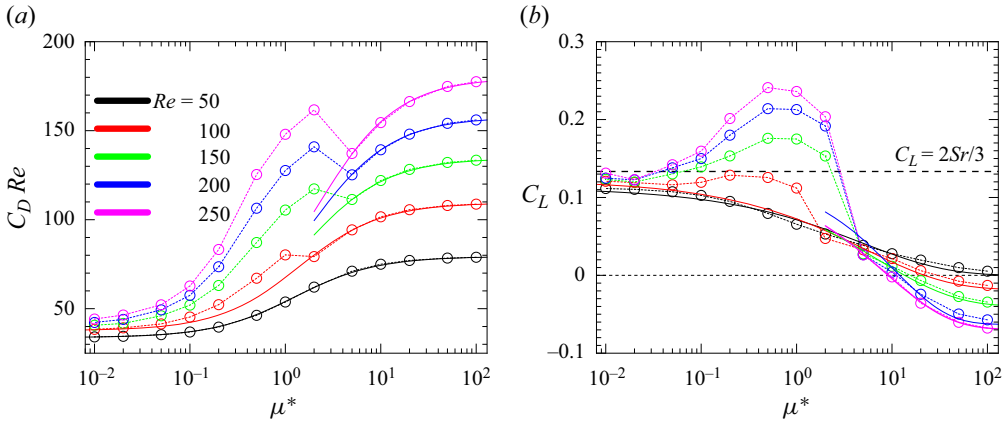
Figure 4. Similar to figure 2, but for $50 \leq Re \leq 250$, $Re^* = 5$ and $Sr = 0.2$. Different colours denote different Re as indicated in panel (*a*). Symbols crossed by dashed lines represent numerical results. In panel (*a*), solid lines denote C_D predictions using (3.3*a*) with m given by (3.4). In panel (*b*), solid lines denote C_L predictions using (3.5)–(3.9*a–e*), horizontal dashed line denotes the lift solution in the inviscid limit (Auton 1987), namely $C_L = 2Sr/3$.

that for a solid sphere, and then gradually decreases as μ^* increases from 2 to 5. At the same Re, C_L attains a local maximum of 0.24 at $\mu^* \approx 0.5$, approximately 1.8 times larger than that predicted by the inviscid solution (Auton 1987), namely $C_L = 2Sr/3$. This latter behaviour is particularly surprising since, as discussed in § 1 and shown in figure 3(*b*), the competition between the 'L' and 'S' mechanisms in generating the lift at $Re = O(100)$ would suggest that: (i) an increase in μ^* should result in a monotonic decrease in C_L and (ii) the maximum C_L should correspond to the inviscid solution and be achieved at the smallest μ^*. Moreover, to the best of our knowledge, no such non-monotonic behaviour in the lift force has been reported until now.

In figure 4, the non-monotonic evolution of C_D and C_L sets in beyond $Re \approx 100$. However, it is not immediately clear whether this Reynolds number dependency is driven by the inertia of the external fluid (i.e. Re) or the internal fluid (i.e. Re^i). So far, the Reynolds number ratio has been fixed at $Re^* = Re^i/Re = 5$, where Re^i is based on the kinematic viscosity of the internal fluid, meaning both Reynolds numbers were varied simultaneously. To clarify the dependency on the internal fluid inertia, additional simulations were conducted at a fixed external Reynolds number of $Re = 200$, varying Re^* from 0.2 to 10. This covers a range for Re^i from 40 to 2000. Given the relation $\rho^* = Re^*\mu^*$, these additional runs also cover a wide range of density ratios, for ρ^* from 10^{-2} to 10^3. The corresponding results for C_D and C_L are summarized in figure 5. These results distinctly demonstrate that it is the inertia of the internal fluid that drives the non-monotonic variation of both $C_D(\mu^*)$ and $C_L(\mu^*)$. Notably, for Re^i smaller than approximately 300 (i.e. $Re^* \lesssim 1.5$), both C_D and C_L depend solely on μ^*, consistent with findings in the low-Re limit (Magnaudet *et al.* 2003). Intriguingly, the computed C_D under this condition aligns well with numerical data at $Sr = 0$ from Feng & Michaelides (2001), which were obtained by imposing the flow to be axisymmetric regardless of μ^*. Conversely, for $Re^i > 300$ (i.e. $Re^* > 1.5$) and μ^* below a critical value μ_c^* that increases with Re^i, the computed C_D and C_L are typically larger than their counterparts in cases where $Re^i \lesssim 300$. The sole exception occurs at $(Re^i, \mu^*) = (2000, 5)$, where C_L is smaller than those at lower Re^i values. These distinct behaviours for $\mu^* < \mu_c^*$ are found to be closely linked to the internal 3-D flow bifurcation, a scenario that will be detailed in § 3.2.
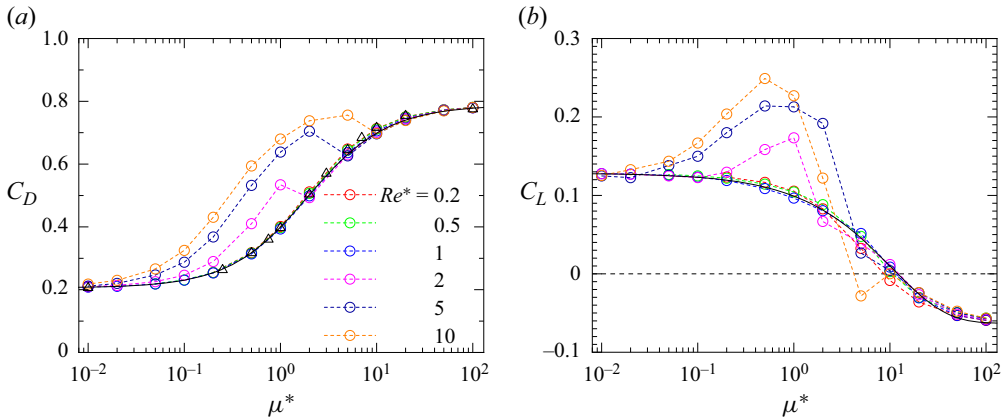
Figure 5. Results for C_D and C_L as a function of μ^* for $0.2 \leq Re^* \leq 10$, $Re = 200$ and $Sr = 0.2$. Different values of Re^* are denoted by different colours as indicated in panel (*a*). The internal Reynolds number is $Re^i = ReRe^*$. In panel (*a*), fitted line, C_D prediction using (3.3*a*) and (3.4); black triangle, data at $Sr = 0$ from Feng & Michaelides (2001) obtained by imposing the flow to be axisymmetric. In panel (*b*), fitted line, C_L prediction using (3.5)–(3.9*a–e*).

3.2. *Identification of the internal 3-D flow bifurcation*

The non-monotonic evolution of $C_D(\mu^*)$ outlined in the preceding section is not exclusive to shear flows. To corroborate this, we conducted additional simulations for droplets with varying viscosity ratios in a uniform flow (i.e. with $Sr = 0$). Figure 6 compares the time histories of C_D obtained at $Sr = 0$ (red dashed line) and $Sr = 0.2$ (red solid line); for both cases, $(Re, Re^*, \mu^*) = (200, 5, 0.5)$. By introducing a time shift $t_0 = 166R/u_{rel}$ and setting $t^* = (t - t_0)u_{rel}/R$ (respectively, $t^* = tu_{rel}/R$) for $Sr = 0$ (respectively, 0.2), the two evolutions almost coincide beyond $t^* \approx 30$. Before this, both cases reach a quasi-steady value of $C_D \approx 0.32$, close to the value reported by Feng & Michaelides (2001) for an axisymmetric flow. These observations suggest a flow bifurcation sets in prior to $t^* \approx 30$, after which the flow becomes strongly non-axisymmetric. This non-axisymmetric flow structure can be visualized using the streamwise vorticity, ω_x, as illustrated in figure 7.

When the ambient flow is uniform ($Sr = 0$), the flow remains axisymmetric prior to the bifurcation (up to $t^* \approx 20$), as indicated by the absence of ω_x structure in figure 7(*a*-i) (corresponding to $t^* = 20$). The flow bifurcation sets in at $t^* \approx 25$, first manifesting as non-axisymmetric flow inside the droplet (figure 7*b*-i), while the external flow retains its axisymmetry. This disturbance grows in time, eventually extending outside the droplet by $t^* \approx 30$ (figure 7*c*-i), peaking in intensity at $t^* \approx 37.5$ (figure 7*d*-i), and then slightly decaying and stabilizing after $t^* \approx 120$ (figure 7*e*-i). Correlating this with the time evolution of C_D in figure 6, a direct link is evident between the drag increase (compared with the drag in the axisymmetric case) and the vortical intensity in the wake. This correlation can be attributed to the 'sucking' effect by the droplet's 3-D wake, where the low-pressure cores of vortical threads increase the pressure difference between the front and back regions of the droplet. Thus, a stronger ω_x in the wake is related to a larger drag increase. Moreover, as the streamwise vorticity structure remains bi-planar symmetric, no lift force is expected on the droplet throughout the process, as confirmed by figure 6 (dashed green line).

In the presence of shear ($Sr = 0.2$), the flow exhibits slight non-axisymmetry prior to the onset of the corresponding imperfect bifurcation. This is evident from the vortical
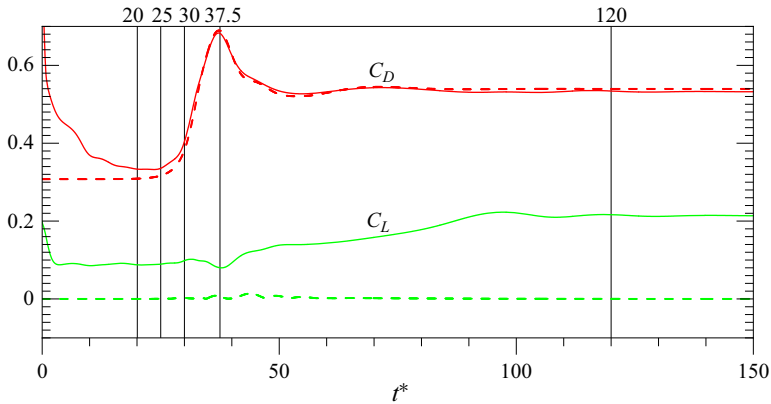
Figure 6. Time history of C_D (in red) and C_L (in green) for $(Re, Re^*, \mu^*) = (200, 5, 0.5)$. Dashed lines, $Sr = 0$; solid lines, $Sr = 0.2$. For $Sr = 0$, a time shift $t_0 = 166R/u_{rel}$ is applied and evolutions are plotted versus the normalized, modified time $t^* = (t - t_0)u_{rel}/R$. For $Sr = 0.2$, no such time shift is applied and $t^* = tu_{rel}/R$. For the case $Sr = 0$, since no flow perturbation was imposed to trigger the bifurcation, C_L is calculated as $C_L = \sqrt{C_y^2 + C_z^2}$, where C_y and C_z are the coefficients of the hydrodynamic force components along y and z, respectively.
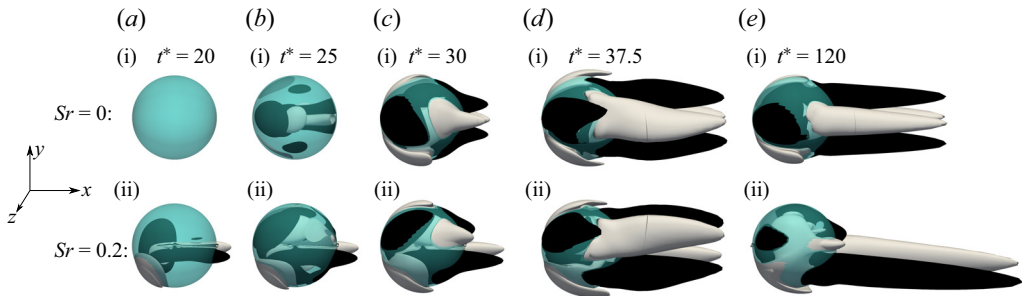

Figure 7. Isosurfaces of the streamwise vorticity $(R/u_{rel})\boldsymbol{\omega} \cdot \boldsymbol{e}_x = \pm 0.5$ in the wake of the droplet for $(Re, Re^*, \mu^*) = (200, 5, 0.5)$ at five selected time points. Panels (i) correspond to $Sr = 0$ and panels (ii) to $Sr = 0.2$. In all panels, negative values are denoted by black threads, while the droplet surface is represented as a partially transparent, light blue-coloured sphere.

structure at $t^* = 20$ (figure 7a-ii), where two streamwise vorticity threads are visible inside and extending outside the droplet in the near wake. Owing to the 'sucking' effect, the drag is slightly higher than in the $Sr = 0$ case. Additionally, the orientation of these vortical threads results in a small but measurable lift force (Auton 1987; Legendre & Magnaudet 1998), as shown in figure 6 (solid green line). Moreover, $C_L = Sr$ at $t = 0^+$ according to figure 6, consistent with the analytical solution derived by Legendre & Magnaudet (1998). As the bifurcation sets in, similar to the $Sr = 0$ case, it is initially the internal flow that shows pronounced non-axisymmetry (figure 7b-ii). This non-axisymmetry intensifies over time, extending outside the droplet by $t^* \approx 30$ (figure 7c-ii), and peaks at $t^* \approx 37.5$ (figure 7d-ii). Interestingly, the ω_x structure at $t^* \approx 37.5$ resembles the bi-planar symmetry seen in the $Sr = 0$ case, which is why the lift at this time moment is even smaller than that before the onset of bifurcation. However, as time progresses, the ω_x threads in the half-space $y > 0$ shrink rapidly, and the reverse is the case for the other two threads, leading the flow to revert to its initial structure with only two significant ω_x threads in the
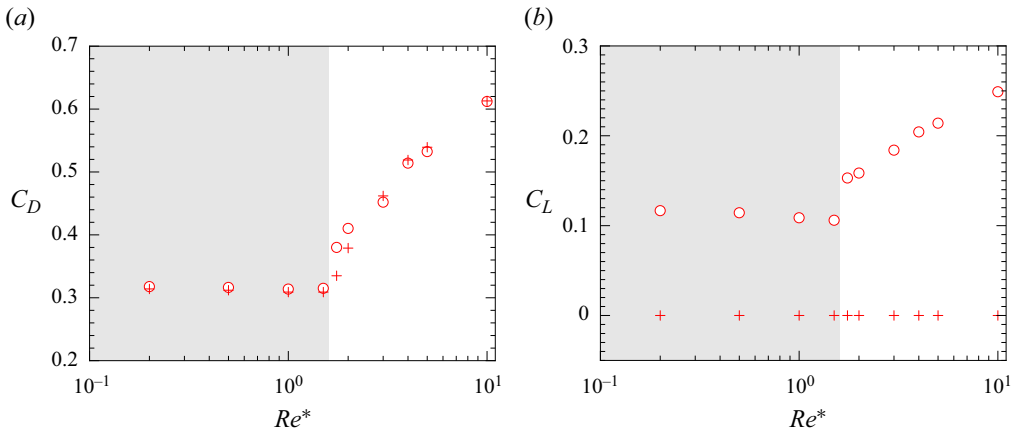
1000 A88-11

(*a*)

(*b*)

Figure 8. Results for C_D and C_L as a function of Re^* for $Sr = 0$ (+, red) and 0.2 (○, red) under the condition $Re = 200$ and $\mu^* = 0.5$. The shaded grey region corresponds to the regime where the flow past the droplet remains axisymmetric for $Sr = 0$.

final stage (compare figure 7*e*-ii with figure 7*a*-ii). Since the intensity of the two vortical threads in the final stage is significantly larger that that before the onset of bifurcation, the lift force is highly increased.

Similar flow characteristics are observed in cases at different Re^*. Figure 8 summarizes the final-state results for C_D and C_L at different Re^*, all obtained at $(Re, \mu^*) = (200, 0.5)$. These results confirm a critical Reynolds number for flow bifurcation at $Re_c^i \approx 300$ (i.e. $Re^* = 1.5$ at $Re = 200$), aligning with findings in figure 5. From these final-state results, and the time evolution of the hydrodynamic forces and flow structures (figures 6 and 7), we conclude that irrespective of the presence of shear, the flow can undergo bifurcation leading to strong non-axisymmetry, marked by multiple threads of streamwise vorticity in the droplet wake. The flow bifurcation identified here differs from that in prior work on a uniform flow past a solid sphere or an oblate spheroidal bubble (Johnson & Patel 1999; Magnaudet & Mougin 2007; Fabre *et al.* 2012; Citro *et al.* 2016), where the internal flow is irrelevant, and bifurcation occurs when the maximum vorticity on the external side of the body surface exceeds a critical, Re-dependent value, say $\omega_c^e(Re)$. Here, internal flow is crucial, as non-axisymmetry initially manifests only within the droplet. Conversely, the external vorticity at the droplet surface, which increase with the viscosity ratio, is not relevant, as the bifurcation only happens for $\mu^* < \mu_c^*$, a regime where the external surface vorticity remains lower than the corresponding ω_c^e. Given these distinct features, we term the phenomenon in our work internal bifurcation, distinguishing it from the external one observed with solid spheres or non-spherical bubbles. The underlying mechanism of this internal bifurcation warrants a further systematic investigation under uniform-flow conditions, which is beyond the scope of the present work. Nevertheless, some preliminary ideas will be provided in § 4.

Before moving to the next section, it is important to highlight another key change in the flow structure before and after the onset of internal bifurcation, due to its close relation to lift generation. To begin, we illustrate in figure 9(*a*-i–*a*-iii) the streamlines for the case $(Sr, Re, Re^*, \mu^*) = (0, 200, 5, 0.5)$ at $t^* = 120$. Four threads of swirling flow can be identified both inside and outside the drop, particularly in the region close to the back surface of the drop. It then becomes clear that the counter-rotating streamwise vortices in the wake originate largely from the swirling flow generated inside the drop during the
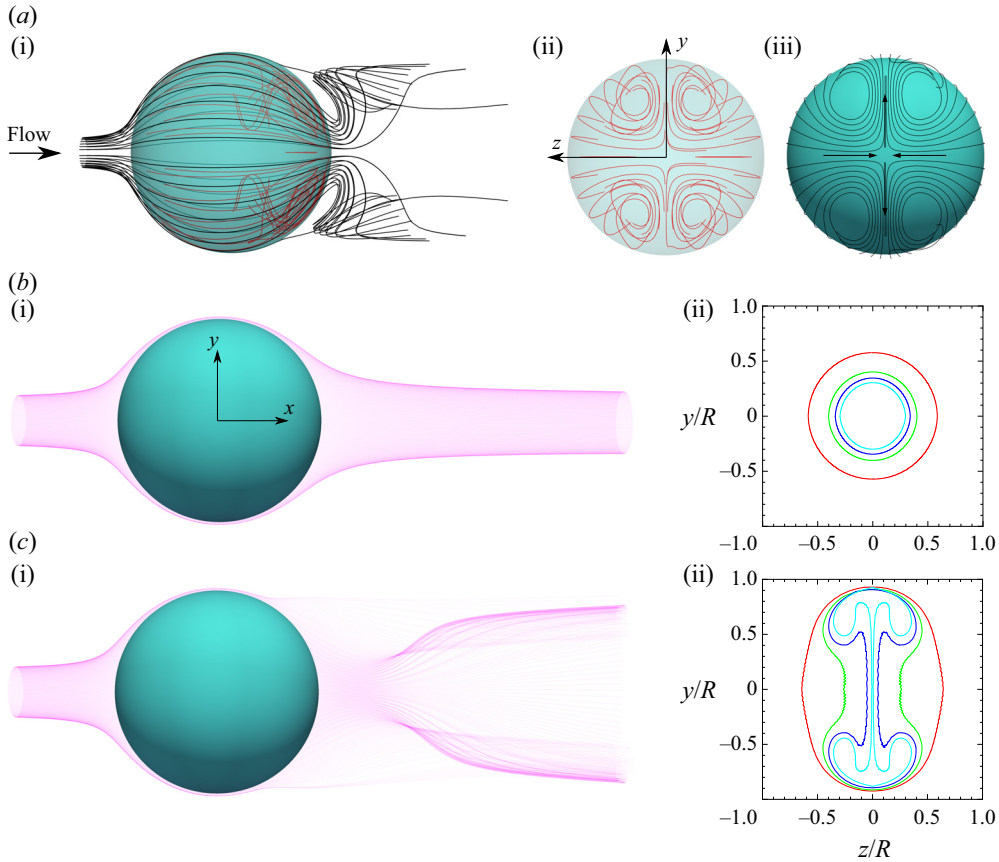
Figure 9. Streamlines and streamtubes for the case $(Sr, Re, Re^*, \mu^*) = (0, 200, 5, 0.5)$. (*a*-i–*a*-iii) Streamlines inside (red) and outside (black) the drop, and close to the back surface of the drop at $t^* = 120$. The coordinates y and z denote the extension and compression directions of the straining flow in the wake, respectively. (*b*-i,*c*-i) Streamtubes formed by all streamlines (coloured in magenta) passing through the circle $[x = -2R, (y^2 + z^2) = (0.25R)^2]$ at $t^* = 20$ and $t^* = 120$, respectively. (*b*-ii,*c*-ii) Corresponding profiles of the streamtube at different distances downstream: red line, $x = R$ green line, $x = 1.5R$; blue line, $x = 2R$; and cyan line, $x = 3R$.

transition from axisymmetric to biplanar symmetric flow. As the swirling flow propagates downstream in the wake, the radial pressure gradient associated with the swirling motion tends to confine the flow, driving the fluid particles towards the centre of each vortical thread. Mass conservation indicates that the flow must accelerate along the streamwise direction, leading to an increase in the extensional rate (i.e. $\partial u_x / \partial x$) in the wake. To highlight this confinement induced by the swirling flow, we compare the streamtubes before ($t^* = 20$) and after ($t^* = 120$) the onset of flow bifurcation. Specifically, we consider the streamtube formed by all streamlines passing through the circle $[x = -2R, (y^2 + z^2) = (0.25R)^2]$. Before the onset of flow bifurcation (figure 9*b*-i–*b*-ii), the cross-stream section of the streamtube remains circular downstream and experiences only moderate confinement for $x \gtrsim 1.5R$. In contrast, after the onset of flow bifurcation (figure 9*c*-i–*c*-ii), the streamtube is highly squeezed, such that the cross-sectional area in the wake is concentrated into the four vortical threads. Specifically, from $x = 2R$ to $x = 3R$, the cross-sectional area decreases from $0.316R^2$ to $0.182R^2$, a relative decrease of approximately 42 %, whereas the relative decrease is only approximately 24 % in the case
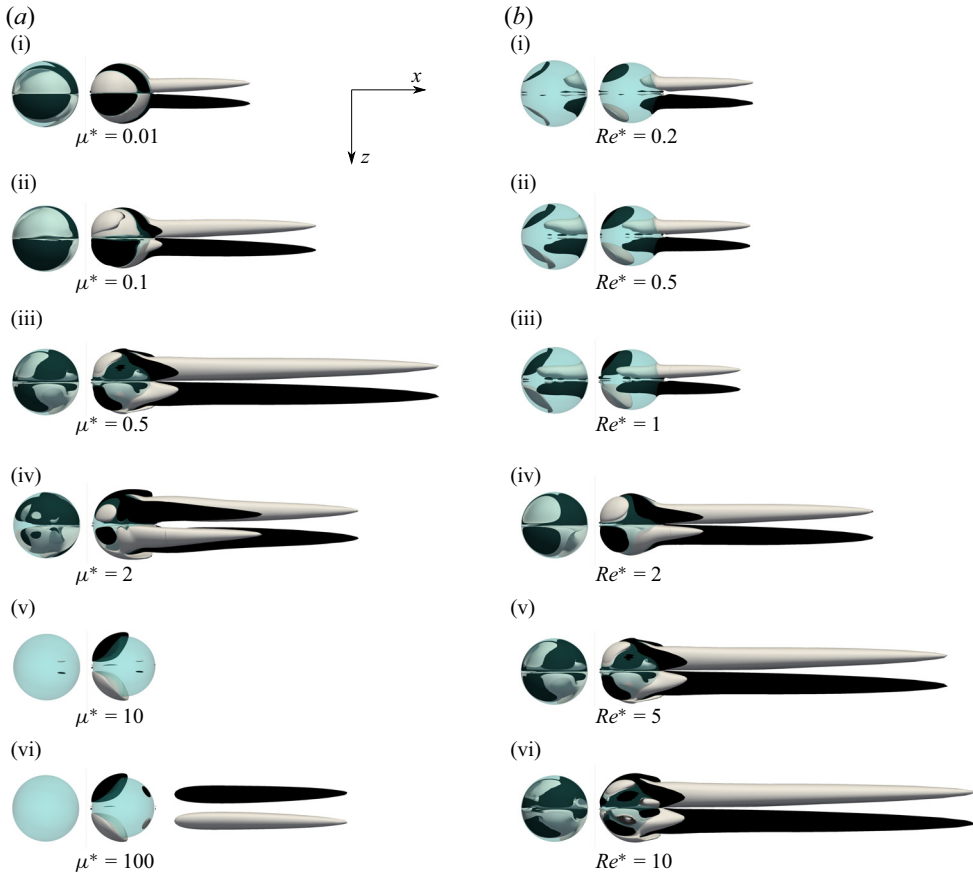
1000 A88-13

Figure 10. Isosurfaces of the streamwise vorticity $(R/u_{rel})\boldsymbol{\omega} \cdot \boldsymbol{e}_x = \pm 0.2$ in the droplet wake (black thread denotes negative values). In each panel, the left part shows only the vortical structure inside the droplet, while the right part shows the vortical structure both inside and outside the droplet. (*a*-i–*a*-vi) Variations at $Re = 200$, $Re^* = 5$, $Sr = 0.2$ for different μ^*. (*b*-i–*b*-vi) Variations at $Re = 200$, $\mu^* = 0.5$, $Sr = 0.2$ for different Re^*.

without the onset of flow bifurcation. This pronounced confinement is closely linked to the amplification of the streamwise vorticity and, hence, to lift generation. The details of this will be discussed in § 3.3.

3.3. *Mechanism of the lift generation at $Re = O(100)$*

3.3.1. *Relation between lift force and streamwise vorticity*

The lift force on a three-dimensional body moving at $Re = O(100)$ is closely related to the presence of a pair of streamwise vortices in its wake (Auton 1987; Legendre & Magnaudet 1998; Adoua *et al.* 2009; Shi *et al.* 2021; Hidman *et al.* 2022). Specifically, the direction of the lift force is determined by the orientations of these vortices. Figure 10(*a*-i–*a*-vi) illustrates the isosurfaces of the streamwise vorticity at various μ^* for $Re = 200$, $Re^* = 5$ and $Sr = 0.2$. The intensity of the streamwise vortices increases as μ^* increases from 0.01, reaching a local maximum at $\mu^* \approx 0.5$, beyond which it starts to decrease. Notably, for $0.1 \leq \mu^* \leq 2$, the vortical intensity is significantly larger than in the clean-bubble limit (figure 10*a*-i). This trend aligns with the behaviour of C_L depicted in figure 4(*b*), where

$C_L(Re = 200)$ peaks at $\mu^* = 0.5$ and remains above the inviscid solution $C_L = 2Sr/3$ for $0.1 \leq \mu^* \leq 2$. As μ^* further increases, the streamwise vortices (figure 10a-iv–a-vi) decrease in intensity, becoming negligible at $\mu^* = 10$, beyond which the sign of the vorticity switches. Correspondingly, the lift coefficient ($C_L(Re = 200)$ in figure 5b) changes its sign at $\mu^* \approx 10$ and remains negative up to $\mu^* = 100$.

Figure 10(b-i–b-vi) presents the same vortical structure but at various Re^* for $Re = 200$, $\mu^* = 0.5$ and $Sr = 0.2$. For $Re^* < 1.5$, the intensity of the streamwise vorticity is nearly independent of Re^* and smaller than that in the clean-bubble limit (figure 10a-i). Consequently, the corresponding C_L (figure 8b) remains smaller than the inviscid solution. However, for $Re^* > 1.5$, the streamwise vortices begin to intensify with increasing Re^*, in line with the gradual increase in C_L in this regime as observed in figure 8(b). Combined with the results for $C_D(Sr = 0)$ shown in figure 8(a), it becomes evident that the internal bifurcation enhances the streamwise vortices, making the lift to exceed the inviscid solution for $Re^* > 1.5$.

Up to this point, the relation between the streamwise vortices and the lift force exerted on a droplet has been only qualitatively confirmed. For a quantitative description, we revisit in Appendix D a simplified model proposed by de Vries, Biesheuvel & van Wijngaarden (2002), later revised and used by Veldhuis (2007) and Zenit & Magnaudet (2009). This model allows the estimation of the lift force from the streamwise vorticity in the wake. We confirm that, provided the streamwise vorticity is known at a cross-stream plane sufficiently far downstream, the lift force can be quantitatively reproduced using the following expression:

$$C_L^{wake} = -\frac{4}{\pi R^2 u_{rel}} \left| \int_{\mathcal{S}} z\omega_x \, \mathrm{d}\mathcal{S} \right| (\boldsymbol{e}_\omega^+ \cdot \boldsymbol{e}_x), \tag{3.1}$$

where C_L^{wake} denotes the lift coefficient estimated from the streamwise vorticity, $\boldsymbol{e}_\omega^+$ denotes the orientation of the vortex in the half-space $z > 0$, and $\mathcal{S}$ represents a surface in the cross-stream plane surrounding one of the streamwise vortices (see figure 22(a) for an illustration of $\mathcal{S}$).

In Appendix D, the relation mentioned above is found applicable in qualitatively reproducing the lift force on a clean bubble. Its applicability in the case of a droplet is assessed in the following. Specifically, figure 11 compares C_L^{wake} with C_L, i.e. the lift coefficient calculated by integrating the pressure and viscous stresses over the interface using (2.6a–c), for a droplet in a linear shear flow of $(Re, Sr) = (200, 0.2)$. It turns out that C_L^{wake}, as per (3.1), matches well with C_L except when $\mu^* > 10$, where C_L^{wake} slightly overestimates the magnitude of the lift force. This mismatch can be understood by noting that in implementing (3.1), the cross-stream plane $\mathcal{S}$ is placed at $10R$ downstream in the wake. Farther downstream, the grid resolution is incapable of fully resolving the vortical structure (for more details, see Appendix D). The comparison in figure 11(a) indicates that while this distance is sufficient to exclude the viscous effects for μ^* up to 10, it probably becomes insufficient at higher μ^*, where the surface vorticity is strong and the associated viscous effects require longer distances downstream to be fully dissipated. Despite this mismatch, the comparison in figure 11 indicates that C_L^{wake} can reproduce the sign reversal of C_L at $\mu^* \approx 10$, as well as the increase in C_L when the flow bifurcation occurs (i.e. when $Re^* \geq 2$).

3.3.2. *Mechanism for the modulation of streamwise vorticity*
Given the close relation between the lift and the streamwise vorticity, understanding the observed lift variation, particularly the increase in lift when the internal bifurcation occurs,
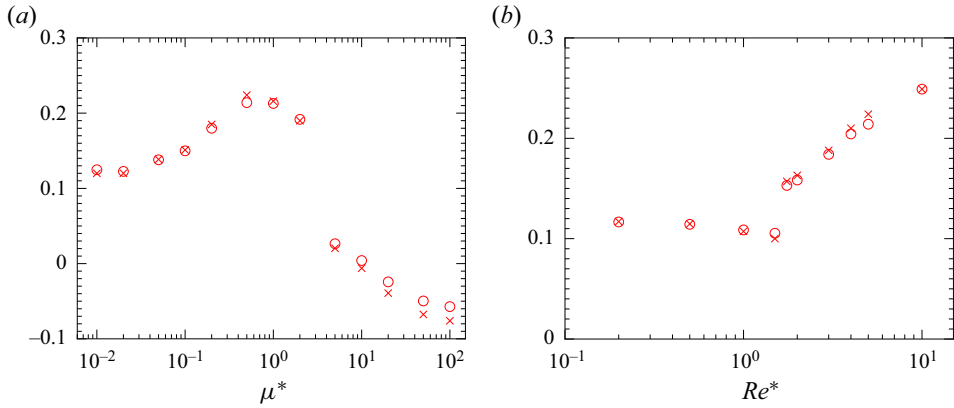
Figure 11. Comparison between the lift coefficient C_L ($\bigcirc$, red) and the vorticity-based lift coefficient C_L^{wake} ($\times$, red) for a droplet across (a) various viscosity ratios and (b) Reynolds number ratios in a linear shear flow with $(Re, Sr) = (200, 0.2)$. (a) $Re^* = 5$; (b) $\mu^* = 0.5$.

necessitates exploring the mechanisms that cause corresponding changes in the streamwise vortices. The generation of streamwise vorticity $\omega_x = \boldsymbol{\omega} \cdot \boldsymbol{e}_x$ is governed by (Adoua *et al.* 2009)

$$\frac{\mathrm{D}\omega_x}{\mathrm{D}t} - \nu\nabla^2\omega_x = \underbrace{\omega_z^\infty \frac{\partial u_x}{\partial z}}_{\text{Source 'L'}} + \underbrace{(\omega_z - \omega_z^\infty)\frac{\partial u_x}{\partial z} + \omega_y\frac{\partial u_x}{\partial y}}_{\text{Source 'S'}} + \underbrace{\omega_x\frac{\partial u_x}{\partial x}}_{\text{Amplification}} , \qquad (3.2)$$

where $\mathrm{D}/\mathrm{D}t = \partial/\partial t + \boldsymbol{u} \cdot \boldsymbol{\nabla}$ represents the material derivative and $u_i = \boldsymbol{u} \cdot \boldsymbol{e}_i$, $\omega_i = \boldsymbol{\omega} \cdot \boldsymbol{e}_i$ (with $i = x, y, z$) are projections along i of the velocity and vorticity, respectively, and $\omega_z^\infty = (\boldsymbol{\nabla} \times \boldsymbol{u}^\infty) \cdot \boldsymbol{e}_z = -\alpha$ denotes the vorticity in the ambient flow.

At $Re = O(100)$, viscous effects become less significant, and the generation of ω_x is primarily influenced by the three terms on the right-hand side of (3.2). The first term, labelled as Source 'L', corresponds to the contribution to the stretching/tilting term, $(\boldsymbol{\omega} \cdot \boldsymbol{\nabla})u_x$, due to the vorticity in the ambient flow. Since the external flow has to accelerate to go around the droplet, $\omega_z^\infty \partial u_x/\partial z = -\alpha\partial u_x/\partial z$ is negative for $z > 0$ (respectively, positive for $z < 0$). The resulting streamwise vorticity, similar to that in figure 10(*a*-i), forms two counter-rotating vortices that entrain the flow within their gap downwards, towards negative y. Consequently, the droplet experiences a lift force directed towards positive y. This inviscid vortex tilting mechanism, documented by Lighthill (1956) and Auton (1987), is hereafter referred to as the '*L*' mechanism. The second term, labelled as Source '*S*', relates to the stretching/tilting term due to the vorticity generated at the droplet surface, $\boldsymbol{\omega}_s$. Regardless of the boundary conditions at the droplet surface, its contribution to $(\boldsymbol{\omega} \cdot \boldsymbol{\nabla})u_x$ always attenuates that by the ambient vorticity $\boldsymbol{\omega}_z^\infty$ and can induce a lift reversal (Legendre & Magnaudet 1998; Adoua *et al.* 2009). This second mechanism is hereafter termed the '*S*' mechanism. Thus, the combination of '*S* + *L*' controls the direction of the lift. The final term on the right-hand side of (3.2) is the interaction of the streamwise vorticity itself with the extensional rate $\partial u_x/\partial x$. Unlike the source terms, this term remains zero if ω_x is absent and serves to amplify it when ω_x is present in the droplet wake.

To gain some insights into the contribution of the three terms in generating the streamwise vorticity before and after the onset of flow bifurcation, we analysed their values at various Re^* for $Re = 200$, $\mu^* = 0.5$ and $Sr = 0.2$. Figure 12(*a*-i–*a*-v) illustrates the corresponding contributions from the combined source '*L* + *S*'. For the cases considered
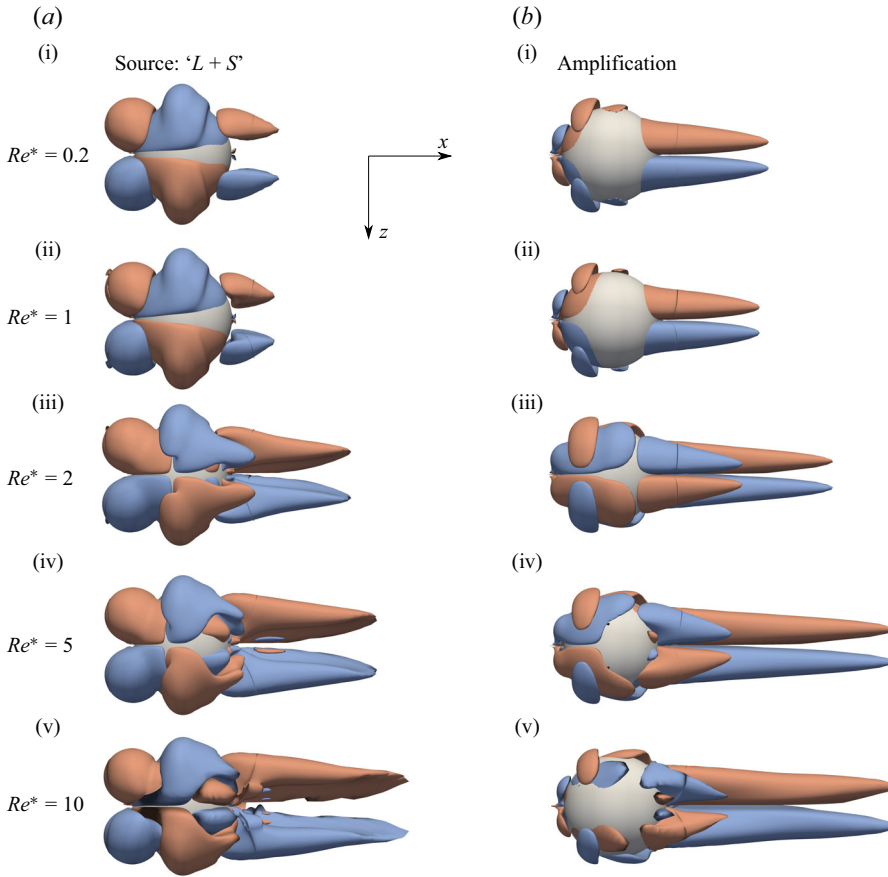
Figure 12. Isosurfaces constructed at values of $\pm 0.1 (u_{rel}/R)^2$ for different ω_x-budgets at $0.2 \leq Re^* \leq 10$, $Re = 200$, $\mu^* = 0.5$ and $Sr = 0.2$. The orange threads denote positive values. (a-i–a-v) Combined source '$L + S$'. (b-i–b-v) Amplification term $\omega_x \partial u_x / \partial x$.

here, the orientation of ω_x in the wake points towards $-x$ for $z > 0$ and towards x for $z < 0$, indicating that the generation of ω_x is largely governed by the L mechanism. Nevertheless, the intensity of the combined source in the wake remains weak for $Re^* < 1.5$. However, in cases where internal bifurcation occurs (i.e. for $Re^* > 1.5$), the combined source in the wake gradually intensifies with increasing Re^*, especially just after the onset of internal bifurcation (compare figure 12a-ii with figure 12a-iii). Figure 12(b-i–b-v) depicts the same isosurfaces but for the amplification term. For $Re^* < 1.5$, amplification is concentrated into two threads, the sign of each closely follows that of the combined source. internal bifurcation takes place at $Re^* \geq 2$. As seen from figure 12(b-iii), the amplification is now concentrated into two pairs of threads: a major pair in the half-space $y < 0$, whose sign follows that of the combined source, and a minor pair in the half-space $y > 0$, displaying a sign opposite to that of the combined source. As Re^* further increases, the minor pair shrinks, nearly disappearing at $Re^* = 10$, while the major pair continuously grows and saturates at $Re^* = 5$. A comparison of the amplification term with the combined source reveals that before the onset of internal bifurcation, the streamwise vortices generated in the wake (figure 10b-i–b-iii) predominantly arise from the amplification term, though their orientations are determined by the combined source. Conversely, after the onset of internal bifurcation (figure 10b-iv–b-vi), both terms actively contribute to the generation of the
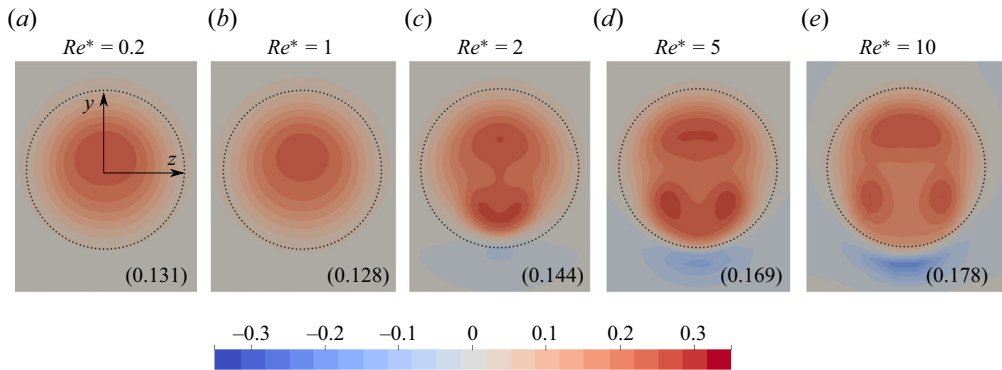
1000 A88-17

Figure 13. Isocontours of the normalized extensional rate $(R/u_{rel})\partial u_x/\partial x$ in the cross-stream plane in the wake at $x = 2R$ downstream of the droplet for $Re = 200$ and $\mu^* = 0.5$, but at different values of Re^* as indicated in the figure. The dashed circle in each panel represents the boundary where $(y^2 + z^2)^{1/2} = R$. In each panel, the number in brackets at the bottom-right indicates the mean value over the surface denoted by the black dashed line, namely the result for $(R/u_{rel})(\pi R^2)^{-1} \int_0^R \partial u_x/\partial x \, 2\pi r \, dr$.

streamwise vorticity. Specifically, the rapid increase in ω_x as Re^* increases from 2 to 5 (compare figure 10b-iv with 10b-v) is largely attributed to the amplification term, since the combined source undergoes only a moderate increase during this phase.

The discussion above indicates in particular that the amplification term experiences a rapid increase due to the onset of internal bifurcation. Referring back to the budget equation (3.2), this implies a rapid increase in the extensional rate $\partial u_x/\partial x$ as a result of the internal bifurcation. This is in line with the discussion in § 3.2, where we confirm that the swirling flow inside the drop leads to strong confinement of the flow downstream in the wake and, hence, an increase in $\partial u_x/\partial x$. Figure 13 illustrates the structures of $\partial u_x/\partial x$ in the cross-stream plane $x = 2R$ at different Re^*. In the absence of the internal bifurcation, i.e. for $Re^* \leq 1.5$, $\partial u_x/\partial x$ exhibits a slight decrease with increasing Re^*. Specifically, its mean value over the surface $y^2 + z^2 \leq R^2$ decreases from 0.131 to 0.128 as Re^* increases from 0.2 to 1 (see the number in brackets at the bottom-right of each panel). As the internal bifurcation occurs, i.e. for $Re^* \geq 2$, its intensity starts to increase with Re^*, reaching 0.178 at $Re^* = 10$. As may be observed from the up-down asymmetry of the contours as the bifurcation sets in, the ambient shear also entrains the flow in the wake downwards, i.e. towards $-y$, making $\partial u_x/\partial x$ more pronounced in the half-space $y < 0$. Given that the two (major) streamwise vortices in the presence of shear are also largely located in this half-space (see figure 7e-ii), the entrainment above leads to a rapid relative increase in the amplification term $\omega_x \partial u_x/\partial x$.

With the insights gained on the effects of internal bifurcation at a fixed μ^*, we now turn our attention to the ω_x-budgets for broader cases where μ^* varies from 0.01 to 100. Starting with the simpler scenarios at $Re^* = 1$ – where, as revealed from figure 5, no internal bifurcation takes place – we assess the contributions of the combined source and the amplification term at various μ^*. These are illustrated in figures 14(a-i–a-vii) and 14(c-i–$c$vii), respectively. For $\mu^* \leq 0.1$, both contributions remain largely unchanged; however, as μ^* increases from 0.1, they start to monotonically decrease and even reverse sign at approximately $\mu^* \approx 10$. Notably, for $\mu^* \geq 2$, the intensity of the combined source becomes negligible in the wake, whereas the amplification term reaches substantial values once μ^* exceeds approximately 10. These findings support the extension of an earlier conclusion concerning the role of amplification, initially drawn from results at $\mu^* = 0.5$, to a wider range of μ^*. They reaffirm that, prior to internal bifurcation, the streamwise
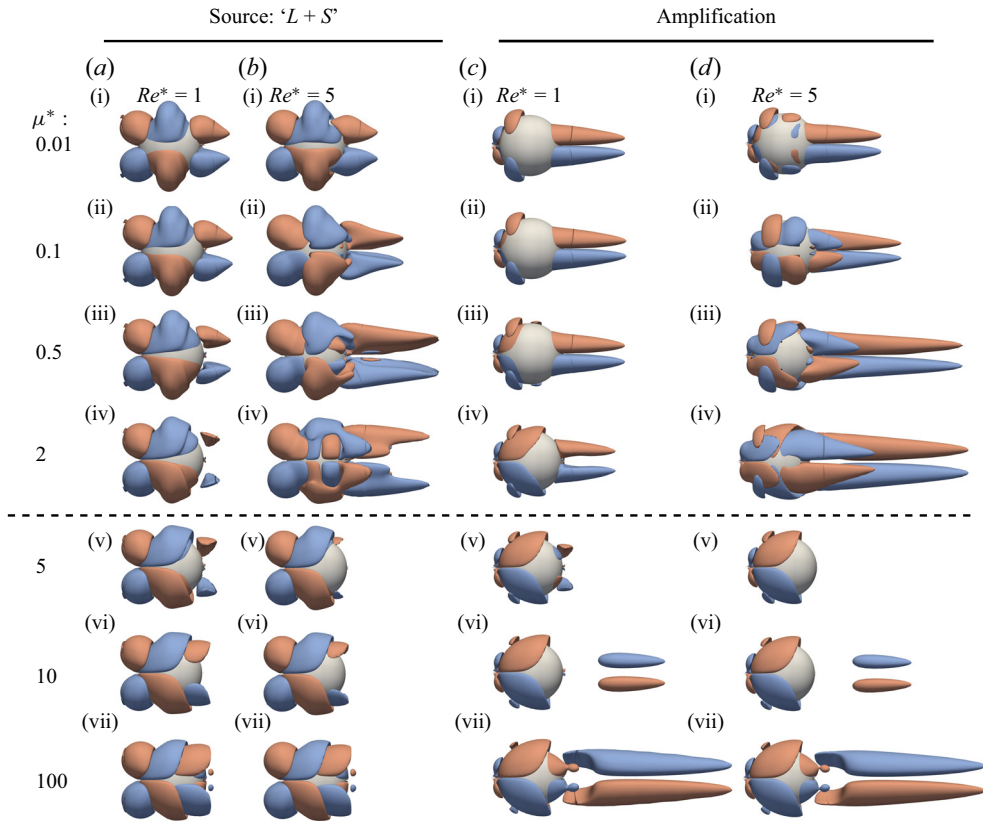
Figure 14. Same as figure 12, but for different viscosity ratios μ^* at two different Reynolds number ratios Re^*.

vortices generated in the wake are predominantly due to the amplification term, although their orientations are determined by the combined source.

Figure 14(b-i–b-vii) (respectively, figure 14(d-i–d-vii) shows the contribution from the combined source (respectively, amplification) under the same conditions as previously discussed, but at a higher Reynolds number ratio, $Re^* = 5$. According to figure 5, no internal bifurcation occurs for $\mu^* \geq 5$. As expected, the contributions from the combined source and amplification exhibit structures identical to their counterparts at $Re^* = 1$. However, for $\mu^* \leq 2$, there are significant deviations from those at $Re^* = 1$. Particularly, for $\mu^* \leq 0.5$, both the combined source and amplification terms experience a sharp increase with increasing μ^*, leading to a rapid augmentation of the streamwise vortices, as observed in figure 10(a-i–a-iii).

Gathering all the information above, a clear picture emerges. For a droplet moving at moderate-to-high Re with an internal Reynolds number Re^i less than a critical value of approximately $Re_c^i = 300$, the lift force acting on the droplet remains independent of Re^i. As μ^* increases, the lift transitions monotonically from the clean-bubble limit ($\mu^* \to 0$), where the lift is positive (i.e. towards $+y$), to the solid-sphere limit ($\mu^* \to \infty$), where the lift is negative. This monotonic transition results from the competition between the 'L' and 'S' mechanisms. The former primarily relies on the ambient vorticity, while the latter also depends on the vorticity generated at the droplet surface, with its intensity increasing alongside μ^* and Re. Consequently, the critical viscosity ratio at which the lift force changes its sign gradually decreases with increasing Re. This sign reversal is
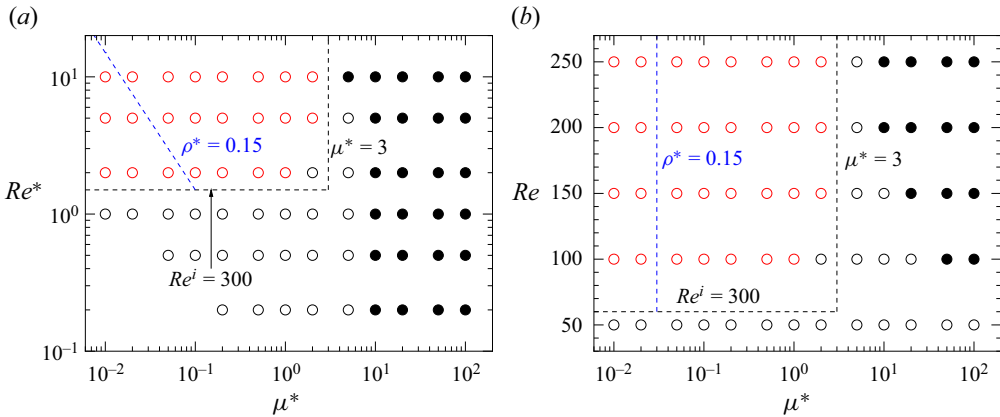
Figure 15. Sign of the lift force in (*a*) the (μ^*, Re^*)-plane for $Re = 200$, and (*b*) the (μ^*, Re)-plane for $Re^* = 5$. Open symbols indicate $C_L > 0$, while solid symbols represent $C_L < 0$. Red open symbols denote cases where the lift is observed to increase due to the onset of internal bifurcation. In each panel, the density ratio increases from left to right, with the dashed blue line denoting $\rho^* = 0.15$.

depicted in figure 15(*b*), which shows the sign of the lift force at $Re^* = 5$ in the phase diagram in terms of (μ^*, Re). Solid (for $C_L < 0$) and open (for $C_L > 0$) symbols are used to distinguish the sign of the lift force.

When the internal Reynolds number surpasses approximately 300, the dynamics change notably. First, in the absence of the ambient shear, an internal bifurcation takes place, causing the flow to transition from axisymmetric to bi-planar symmetric, as outlined in § 3.2. This transition is accompanied with a swirling flow inside the drop, which squeezes the flow in the wake (figure 9) and, hence, increases the extensional rate $\partial u_x / \partial x$ therein. Then, in the presence of shear, the amplification term in the ω_x-budget equation (3.2) increases, due to the enhanced extensional rate $\partial u_x / \partial x$. This increase intensifies the streamwise vorticity generated in the droplet wake (figures 10, 12 and 14), causing the lift force to exceed its counterpart in cases with $Re_c^i \leq 300$ and, in some cases, even surpass the value in the inviscid limit (figures 4*b*, 5*b* and 8*b*). However, even when Re^i exceeds 300, the internal bifurcation is found to disappear for approximately $\mu^* \geq 5$ (figure 14), and thus the pattern of lift reversal, typically occurring at $\mu^* \approx 10$, remains unaffected by Re^i up to $Re^i = 1000$ (figure 15*a*). Nevertheless, at the highest internal Reynolds number considered in this work ($Re^i = 2000$), we do observe some deviation in lift reversal behaviour. Specifically, the lift is already negative at $\mu^* = 5$ (figures 5*b* and 15*a*), while it remains positive for all other cases where $Re^i \leq 1000$. To unravel the mechanism behind the premature lift reversal at this high Re^i, we examine various flow structures under this condition in Appendix C. It turns out that the combined source downstream in the wake is predominantly positive for $z > 0$, contrasting the corresponding case at $Re^i = 200$. This suggests that the internal bifurcation at high Re^i significantly enhances the 'S' mechanism, while primarily augmenting the 'L' mechanism for cases with $Re^i \leq 1000$.

To close this subsection, we have compiled in figure 15 the cases (denoted by red open symbols) where an increase in lift is observed due to the onset of internal bifurcation. These results indicate that, in addition to requiring $Re^i > 300$, the viscosity ratio must be smaller than a critical value, approximately $\mu_c^* = 3$, for such an increase in lift force to occur. However, as already shown in figures 4 and 5, the lift increase remains modest at low μ^*, especially when the Reynolds number ratio Re^* is small. A closer inspection of cases where $\mu^* \leq 1$ reveals that the difference between the lift in the final state and that in

the quasi-steady state prior to the onset of internal bifurcation (as illustrated in figure 6) is less than 5 % when $\rho^* \approx 0.15$. Moreover, this difference diminishes with a decrease in ρ^*. Given this trend, it is not surprising that for a gas bubble rising in liquid where $\mu^* \to 0$ and $Re^i > 300$, while internal bifurcation may still occur, the induced modifications in the drag and lift forces remain negligible as $\rho^* \to 0$.

3.4. *Influence of the relative shear rate*

For all the shear-flow cases discussed above, the relative shear rate is fixed at $Sr = 0.2$. The influence of Sr will be discussed in this section. In the low-to-moderate Reynolds number regime, as indicated in § 3.1, the computed lift and drag to leading order can be satisfactorily predicted using the low-Re expression. This suggests that the generation of both forces is still governed by the vortical mechanism (Legendre & Magnaudet 1998; Magnaudet 2003). More specifically, the drag is directly proportional to the strength of the vorticity generated at the droplet surface, while the lift results from: (i) the non-zero surface vorticity diffusion and (ii) the asymmetric advection produced by the shear. Hence, in addition to the dependency on ω_s outlined in § 3.1, while the drag force is only weakly influenced by Sr, the lift force is proportional to $Sr^{1/2}$, provided that $Sr \leq O(0.1)$. These Sr-related features have been confirmed in prior work concerning spherical bubbles (Legendre & Magnaudet 1998; Shi *et al.* 2020) and solid spheres (Kurose & Komori 1999; Bagchi & Balachandar 2002; Shi *et al.* 2021) in linear shear flow for Sr up to 0.5 or even higher.

At $Re = O(100)$, it is interesting to see how the ambient shear affects: (i) the onset of internal bifurcation at low-to-moderate viscosity ratio μ^* and (ii) the sign reversal of the lift force which occurs at relatively larger μ^*. For this purpose, we conducted two additional series of simulations, one at $Sr = 0.02$ and the other at $Sr = 0.5$. In both series, we fixed $(Re, Re^*) = (200, 5)$ but varied the viscosity ratio from 0.01 to 100. Figure 16 illustrates the variation of the obtained C_D and C_L (together with those at $Sr = 0.2$) as a function of μ^*. Recall that the onset of internal bifurcation is accompanied by an increase in C_D; the results in figure 16(*a*) indicate that the critical viscosity ratio, μ_c^*, below which the internal bifurcation sets in, is between 2 and 5 for $Sr \leq 0.2$ and between 5 and 10 for $Sr = 0.5$. Moreover, in the regime where $\mu^* \leq 2$ and internal bifurcation occurs at all three considered Sr values, the calculated C_D at a given μ^* experiences a slight increase with Sr for $Sr \geq 0.2$. This shear-induced drag increase is not directly linked to the internal bifurcation. Rather, it results from the interaction between the ambient vorticity and the velocity disturbance associated with the streamwise vortices in the wake. The resulting drag increase, say, $\Delta C_D = C_D(Sr \neq 0) - C_D(Sr = 0)$, is proportional to Sr^2 and Sr in the limits $\mu^* \to 0$ (Legendre & Magnaudet 1998; Shi *et al.* 2020) and $\mu^* \to \infty$ (Kurose & Komori 1999; Shi *et al.* 2021), respectively. Nevertheless, for $0.1 < \mu^* < \mu_c^*$, the drag increase arises largely from the internal bifurcation even at $Sr = 0.5$ (comparing the data points with the solid line in figure 16), indicating that the shear-induced drag increase is only of secondary importance. Piecing together the information above, it may be concluded that the ambient shear promotes the internal bifurcation by increasing the threshold viscosity ratio below which the internal bifurcation can occur, yet it does not strongly affect the resulting drag increase.

Figure 16(*b*) illustrates the variation of C_L with increasing μ^*. For all three shear rates, C_L reverses from positive to negative at $\mu^* \approx 10$, indicating that the lift reversal is not influenced by the intensity of the ambient shear. To understand this feature, let us revisit the budget equation of ω_x, namely, (3.2). In a cylindrical coordinate system (r, ϕ, x), the droplet surface may be considered as a vortex sheet with $\boldsymbol{\omega}_s = \omega_\phi \boldsymbol{e}_\phi$, provided that the
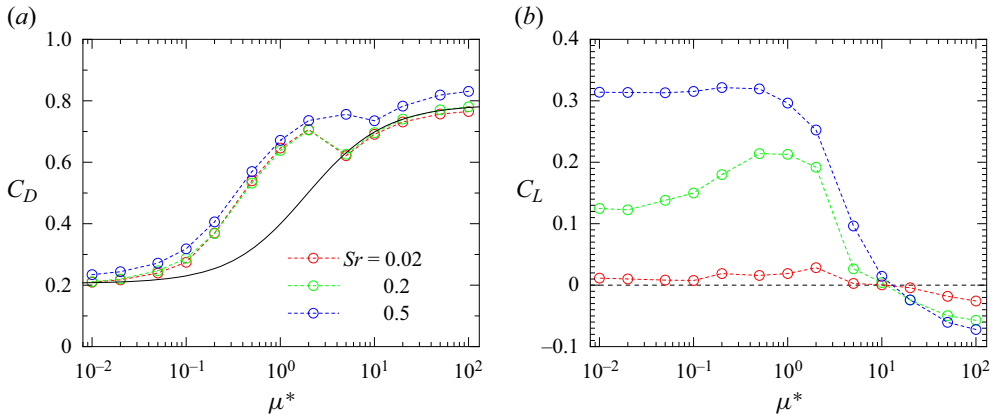
Figure 16. Results for C_D and C_L against μ^* at $(Re, Re^*) = (200, 5)$ for different Sr. In panel (a), the black solid line denotes C_D prediction using (3.3a) and (3.4).

ambient shear is not too strong (i.e. for $Sr \leq O(0.1)$) such that the base flow remains largely axisymmetric. Then, the 'S' source term, which now takes the form $\omega_\phi \partial u_x/(r\partial\phi)$, is of $O(Sr\omega_\phi(u_{rel}/R))$ because u_x varies by $2\alpha R$ over one droplet diameter. However, the 'L' source term is of $O(Sr\partial u_x/\partial z(u_{rel}/R))$. Given that both terms are proportional to Sr, the critical viscosity ratio characterizing the lift reversal depends largely on the difference in the intensity of the spanwise gradient $\partial u_x/\partial z$ and the azimuthal vorticity ω_ϕ in the corresponding uniform base flow, and is minimally influenced by the ambient shear.

Another interesting feature revealed in figure 16(b) is the distinct profiles of $C_L(\mu^*)$ at the three different Sr for $\mu^* \leq \mu_c^*$. Specifically, it is only in the moderate shear rate case ($Sr = 0.2$) that the lift variation is strongly influenced by the internal bifurcation. To better understand the interaction between the ambient shear and the velocity disturbance associated with the internal bifurcation, we present in figure 17 the structure of the streamwise vorticity at $\mu^* = 0.5$ for Sr increasing from 0 to 0.5. Note that the view direction is $-e_z$, so that the level of up-down asymmetry characterizes the magnitude of the wake-induced lift. At $Sr = 0$, the vortical structure remains up-down symmetric, in line with the zero lift for this case seen in figure 8(b). With the presence of a weak shear ($Sr = 0.02$), asymmetry sets in such that the upper vortex pair shrinks slightly, and the reverse is the case for the vortex pair in the half-space $y < 0$. As outlined in § 3.3.2, this change in the vortical structure is linked to the entrainment of the droplet wake by the ambient shear, which causes a redistribution of vorticity intensity, enhancing the lower vortex pair at the expense of the upper one. This redistribution is the key mechanism responsible for the lift re-increase as the internal bifurcation sets in. At $Sr = 0.2$ and 0.5, the upper vortex pair disappears, indicating that the redistribution process saturates at $Sr_c \leq 0.2$. This saturation can also be observed by examining the lift increase caused by the internal bifurcation, say, C_L^{Bi}, for these two cases. By examining the time evolution of the lift coefficient, it is observed that C_L after the internal bifurcation sets in increases from 0.11 to 0.21 at $Sr = 0.2$ (see figure 6) and from 0.22 to 0.32 at $Sr = 0.5$ (without figure), indicating $C_L^{Bi} = 0.1$ for both cases. Hence, once the ambient shear is strong enough for the redistribution process to saturate, the lift increase due to bifurcation depends only on the corresponding uniform base flow (hence on (Re, Re^*, μ^*)) and is not directly linked to the ambient shear. Piecing together the information above, the $C_L(\mu^*)$ evolution in the internal bifurcation regime depends on two parameter ratios: (i) Sr/Sr_c, which measures
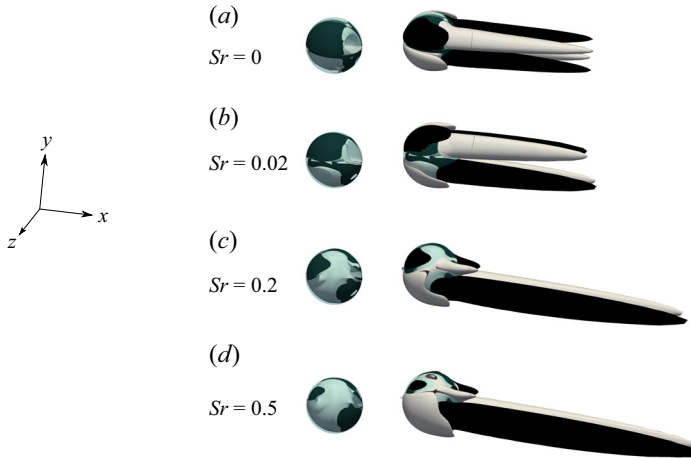
Figure 17. Isosurfaces of the streamwise vorticity $(R/u_{rel})\boldsymbol{\omega}\cdot\boldsymbol{e}_x = \pm 0.2$ in the droplet wake (black thread denotes negative values) for different Sr. For all cases, $\mu^* = 0.5$ and $(Re, Re^*) = (200, 5)$.

the relative intensity of the ambient shear Sr with respect to the threshold shear rate Sr_c characterizing the saturated bifurcation and (ii) $C_{L,0}/C_L^{Bi}$, which measures the relative magnitude of the base-flow lift (proportional to Sr) with respect to the bifurcation-induced lift (independent of Sr). Specifically, the evolution of $C_L(\mu^*)$ is strongly affected by the internal flow bifurcation only if $Sr/Sr_c = O(1)$ and $C_{L,0}/C_L^{Bi} \leq O(1)$. This is because, for $Sr \ll Sr_c$, the shear–wake interaction remains weak such that the flow structure remains nearly bi-planar symmetric (comparing, e.g. figures 17a and 17b). However, for $C_{L,0}/C_L^{Bi} \gg 1$, the disturbance flow associated with the internal bifurcation is too weak to affect the flow structure in the quasi-steady state prior to the onset of bifurcation (comparing, e.g. figures 17a and 17d).

3.5. *Drag and lift expressions obtained from the numerical data*

Based on the numerical data from the present work and prior asymptotic predictions established in the low- or high-Reynolds-number limits, we propose in this section semiempirical expressions for the drag and lift forces that are valid over a wide range of Reynolds numbers and viscosity ratios, provided that $Sr \leq 0.5$.

At low Reynolds numbers, analytical solutions at leading order for the drag and lift forces were derived by Legendre & Magnaudet (1997) and Magnaudet *et al.* (2003) using a matched asymptotic expansion procedure. Building on these prior results, the drag and lift force coefficients, C_D and C_L, for a droplet with arbitrary viscosity ratio μ^* can be proposed based on the values in the limits of $\mu^* \to 0$ and $\mu^* \to \infty$:

$$C_D(\mu^*) = C_D^B + (R_\mu^m - 1)\frac{C_D^S - C_D^B}{(3/2)^m - 1}; \tag{3.3a}$$

$$C_L(\mu^*) = C_L^B + (R_\mu^2 - 1)\frac{C_L^S - C_L^B}{(3/2)^2 - 1}, \tag{3.3b}$$

where $R_\mu = (2 + 3\mu^*)/(2 + 2\mu^*)$ denotes the Stokeslet variation with μ^* and $m = 1$ for $Re \ll 1$. Here, C_L^B (respectively, C_D^B) and C_L^S (respectively, C_D^S) represent the lift

(respectively, drag) coefficients in the clean-bubble ($\mu^* \to 0$) and solid-sphere ($\mu^* \to \infty$) limits, respectively.

The low-Re predictions using (3.3) appear in figure 2 as black solid lines. The leading-order solution for C_L in the small and large viscosity ratio limits is also shown (blue lines in panel *b*). The predicted C_D from (3.3*a*) with $m = 1$ shows good agreement with the numerical data. Regarding C_L, at $\mu^* = 100$, our numerical data yield $C_L = 2.94$, slightly lower than the leading-order solution (in terms of $(SrRe)^{1/2}$) for a solid sphere (Saffman 1965; McLaughlin 1991; Legendre & Magnaudet 1997; Candelier, Mehlig & Magnaudet 2019), which gives $C_L^{S(1)} = 3.13$. However, considering the second-order inertial lift correction of $\Delta C_L^{S(2)} = -0.504 Sr$ from recent analysis (Candelier *et al.* 2023) (see (B3) in Appendix B), our numerical result differs from the refined low-Re solution $C_L^{S(2)} = C_L^{S(1)} + \Delta C_L^{S(2)}$ by only approximately 5 %. The trend of $\Delta C_L^{(2)}(\mu^*)$ as μ^* decreases is not fully understood. Nevertheless, at $\mu^* = 0.01$, C_L according to our numerical results is 1.35, which aligns closely with the leading-order low-Re solution for a spherical clean bubble, $C_L^{B(1)} = 1.39$ ((B4*b*) in Appendix B). This suggests that the second-order correction becomes negligible at low μ^*. Thus, for intermediate μ^*, it seems feasible to approximate C_L using (3.3*b*) together with C_L^B and C_L^S approximated using $C_L^{B(1)}$ and $C_L^{S(2)}$, respectively, as confirmed in figure 2(*b*).

As Re increases from 0.2, the ratio C_D^S/C_D^B increases from 1.6 at $Re = 1$ to 3.7 at $Re = 250$ according to the numerical data, indicating that the low-Re expression for C_D with $m = 1$ no longer applies when $Re \geq O(1)$. The increase in C_D^S/C_D^B can be attributed to two phenomena: (i) the surface vorticity ω_s increases with Re for $Re \geq O(1)$ and (ii) the evolution of $\omega_s(Re)$ is dependent on μ^*. Specifically, $\omega_s \propto Re^{1/2}(u_{rel}/R)$ in the solid-sphere limit for $Re \geq 10$ (Magnaudet *et al.* 1995), whereas $\omega_s \to 3(u_{rel}/R)$ in the clean-bubble limit beyond $Re \approx 100$ (Legendre 2007). Based on the present numerical data up to $Re = 250$, we propose the following fitted expression for the exponent m in (3.3*a*):

$$m(Re \geq O(1)) = 1 + 0.01 Re^{1.1}. \tag{3.4}$$

As figure 3(*a*) and 4 show, the simple drag model based on (3.3*a*) and (3.4) satisfactorily reproduces the numerical data for all considered μ^*, provided that no internal flow bifurcation takes place.

As for the lift force, the low-Re expression for C_L is capable of reproducing the numerical data qualitatively up to $Re = 20$ (solid lines in figure 3*b*). For $Re \geq 20$, an approximate expression inspired by the competition between the 'L' and 'S' mechanisms is proposed as follows:

$$C_L(\mu^*, Re \geq 20) \approx C_L^B g_L + C_L^S(1 - g_L), \tag{3.5}$$

with

$$g_L(\mu^*, Re) = \exp[-A(Re)(\mu^*)^{B(Re)}], \tag{3.6}$$

where

$$A(Re) = \sum_{n=0}^{4} a_n \left(\frac{Re}{100}\right)^n \quad \text{and} \quad B(Re) = \sum_{n=0}^{4} b_n \left(\frac{Re}{100}\right)^n. \tag{3.7a,b}$$

The coefficients of a_n and b_n in (3.7*a,b*) are fitted based on the numerical data for $Re \geq 20$, resulting in

$$a_0 = 1, \quad a_1 = -2.2, \quad a_2 = 3, \quad a_3 = -1.7, \quad a_4 = 0.32, \tag{3.8a-e}$$

and

$$b_0 = -0.5, \quad b_1 = 4, \quad b_2 = -5.4, \quad b_3 = 2.9, \quad b_4 = -5.2. \qquad (3.9a\text{–}e)$$

The predictions using (3.5)–(3.9a–e) appear as solid lines in figure 4(b).

4. Summary and final discussion

4.1. *Main findings*

We have carried out comprehensive 3-D simulations of a linear shear flow past a spherical droplet over a wide range of external Reynolds numbers (Re) and drop-to-fluid viscosity ratios (μ^*). Our primary focus is on the hydrodynamic forces, especially the lift force, acting on the droplet in the quasi-steady flow limit. In this context, we have dedicated significant effort to understanding how the lift force transitions from the clean-bubble limit ($\mu^* \to 0$) to the solid-sphere limit ($\mu^* \to \infty$) at both low and high Reynolds numbers. For most of our simulations, we maintained a constant dimensionless shear rate at $Sr = 0.2$ and a fixed ratio of the internal Reynolds number (Re^i) to the external one (Re) at $Re^* = 5$. The key findings from these simulations are summarized as follows.

In the low (external)-Reynolds-number regime, prior work adopting matched asymptotic expansions (Legendre & Magnaudet 1997; Magnaudet *et al.* 2003) indicated that the lift on a droplet is proportional to ω_s^2, the square of the maximum vorticity generated at the droplet surface, while the drag is proportional to ω_s. Particularly, this leads to the conclusion that the ratio of lift (drag) in the solid-sphere limit to that in the clean-bubble limit is $(3/2)^2$ (respectively, $3/2$) for $Re \ll 1$. Our numerical results align closely with these theoretical predictions up to $Re \approx 0.5$, as demonstrated in figures 2 and 3.

At moderate-to-high external Reynolds numbers, provided that the internal Reynolds number is smaller than a critical value of $Re_c^i \approx 300$, the drag and lift forces at a given Re are determined solely by the viscosity ratio μ^*, consistent with the low-Re theory (Legendre & Magnaudet 1997; Magnaudet *et al.* 2003). Within this regime, our numerical results for drag still follow the predictions of the low-Re theory up to $Re = 250$, the maximum Re considered in this study, provided that finite-Re corrections to the surface vorticity ω_s are reasonably accounted for (figures 3, 4 and 5). However, the evolution of the lift force with increasing μ^* significantly deviates from the low-Re theory, which suggests a gradual increase in the lift coefficient C_L with increasing μ^*. Notably, at $Re = 2$, C_L exhibits only a weak dependence on μ^* (figure 3b). Beyond this point, C_L progressively decreases with increasing μ^* (figures 3, 4 and 5). This gradual decrease results from a competition between two distinct mechanisms responsible for the lift generation at high Reynolds numbers. The first, known as the 'L' mechanism (Lighthill 1956; Auton 1987), largely depends on the ambient vorticity and yields a positive lift contribution, parallel to that predicted by the low-Re theory. The second is the so-called 'S' mechanism (Adoua *et al.* 2009) which depends in addition on the maximum surface vorticity ω_s and contributes to a negative lift force. The interplay between these two mechanisms leads to a decrease in the combined lift force with increasing μ^* and a change in its sign beyond a critical, Re-dependent μ^* (figure 15).

Still at moderate-to-high external Reynolds numbers, things become different when Re^i exceeds approximately 300. Notably, for droplets with a viscosity ratio lower than approximately $\mu_c^* = 3$, an internal bifurcation occurs (see § 3.2). This leads to a strongly non-axisymmetric disturbed flow, characterized by multiple threads of streamwise vorticity in the wake downstream. In cases where this internal bifurcation takes place, the hydrodynamic forces exerted on the droplet are substantially altered. Particularly, the drag increases due to the 'sucking' effect caused by the droplet's 3-D wake. We confirm that this

increase in drag is nearly independent of the presence of shear, provided that $Sr \leq O(0.1)$. Conversely, the effect on the lift force is shear dependent. Without shear ($Sr = 0$), the flow after the onset of internal bifurcation remains bi-planar symmetric and hence no lift is generated. However, with the presence of shear, the internal bifurcation significantly enhances the two threads of streamwise vorticity formed before the onset of bifurcation, leading to a notable increase in lift force. The underlying mechanism for this increase in lift was further detailed in § 3.3. First, we established in § 3.3.1 (also see Appendix D) a close relationship between the lift force and the streamwise vorticity, ω_x, in the wake of the droplet. Subsequently, in § 3.3.2, we examined the impact of the internal bifurcation on the generation of ω_x. It was demonstrated that the internal bifurcation is marked by a significant increase in the extensional rate $\partial u_x / \partial x$ (figures 9 and 13). This amplifies the ω_x generation (see (3.2)) irrespective of μ^* (figures 14 and 10), thereby resulting in a substantial increase in the lift acting on the droplet.

Based on these findings, we discussed in § 3.4 the influence of the shear rate Sr at $Re = O(100)$, using results above together with those from additional runs at $Sr = 0.02$ and 0.5. These results indicate that C_D is only weakly affected by Sr, provided that the ambient shear remains not too strong, roughly for $Sr \leq 0.5$. However, the lift reversal occurs at $\mu^* \approx 10$ irrespective of Sr, as both the 'L' and 'S' source terms depend linearly on Sr. Moreover, in the regime $\mu^* \leq \mu_c^*$ where a 3-D internal flow bifurcation sets in, the resulting lift re-increase seems to saturate at $O(Sr_c)$ when the ambient shear exceeds a critical shear rate Sr_c. Hence, provided that $Sr \gg Sr_c$, the lift force may still exhibit a monotonic transition from $\mu^* \to 0$ to $\mu^* \to \infty$ even with the onset of internal flow bifurcation.

Present work improves the current understanding of the mechanisms driving the evolution of the lift force in relation to the viscosity ratio μ^*, particularly illustrating how the transition from the clean-bubble limit ($\mu^* \to 0$) to the solid-sphere limit ($\mu^* \to \infty$) varies across different Reynolds numbers (Re). From a practical point of view, this study also offers empirical models for the drag [(3.3a) and (3.4)] and the lift [(3.3a) and (3.5)–(3.9a–e)] forces acting on spherical droplets. These models are valid at arbitrary μ^* for Re up to 250, provided that the internal bifurcation does not take place. These empirical models can be used in point-particle simulations to estimate the dispersion of droplets in droplet-laden flows.

4.2. *Discussion*

One issue that deserves further discussion is the fundamental question concerning the theoretical prediction of the flow bifurcation occurring when the internal Reynolds number exceeds a critical value of approximately 300. As corroborated in § 3.2 and by previous findings of Edelmann *et al.* (2017) and Rachih (2019), this notable shift in flow structure already emerges in the corresponding uniform-flow conditions. In the presence of shear, the critical Re^i characterizing the (imperfect) bifurcation appears to be only marginally influenced by the shear rate. While the underlying mechanism for the internal bifurcation remains unclear, some hints may be inferred from the mechanism for the external bifurcation of the flow past rigid bodies whose surfaces obey either free-slip or no-slip conditions. In that case, external bifurcation sets in only when the surface vorticity generated at the external side of the body, say ω^e, exceeds a critical value that depends on the (external) Reynolds number Re (Magnaudet & Mougin 2007). In analogies to the external bifurcation, we believe the existence of a close relation between the maximum vorticity at the internal side of the droplet surface, say ω^i, and the onset of internal bifurcation, and anticipate that internal bifurcation sets in once ω^i exceeds a critical value

that depends on the internal Reynolds number Re^i. To corroborate this, let us first check how ω^i varies with the viscosity ratio μ^* at $Re = O(100)$. At steady state, continuity of velocity and tangential stress across the interface yields the following relation between the internal (ω^i) and external vorticity (ω^e) at the droplet surface:

$$\omega^i = \frac{1}{\mu^*}\left[\omega^e - 2\frac{u_s}{R}(1 - \mu^*)\right], \tag{4.1}$$

where u_s denotes the local tangential velocity at the interface (see, e.g. Magnaudet & Mougin (2007) for the detailed definition). This relation indicates that, for a fixed external vorticity, the internal vorticity increases as the viscosity ratio decreases. Taken together with our hypothesized cause of the internal bifurcation, there must exist a critical internal surface vorticity, denoted ω_c^i, which is reached as μ^* decreases to μ_c^*, such that $\omega^i \geq \omega_c^i$ for $\mu^* \leq \mu_c^*$. This is in line with the findings revealed from the present work. Moreover, the fact that internal bifurcation sets in only when $Re^i > 300$ simply means that ω_c^i increases with decreasing Re^i such that it requires a very large ω^i to trigger the internal bifurcation for $Re^i \leq 300$, and this large ω^i is not achieved in the range of parameters considered in this work, probably owing to the still small external Reynolds number considered in this work. Verifying the above speculation will likely require an extensive numerical study of the flow around the critical bifurcation point in the uniform-flow condition, accompanied by the development of a suitable linear stability analysis approach.

Declaration of interests. The authors report no conflict of interest.

Author ORCIDs.

Pengyu Shi https://orcid.org/0000-0001-6402-4720;

Éric Climent https://orcid.org/0000-0001-9538-338X;

Dominique Legendre https://orcid.org/0000-0002-6021-7119.

Appendix A. Preliminary tests

In our initial series of tests, we assessed the drag and lift forces acting on a spherical droplet at a shear rate of $Sr = 0.2$, particularly for extreme viscosity ratios $\mu^* = 0.01$ and $\mu^* = 100$. Considering the requirement for continuous tangent stress at the interface (as per (2.3c)), we expect that the hydrodynamic forces on the droplet will approximate those on a clean bubble (which has a shear-free surface) at low μ^*, and those on a solid sphere (with a no-slip surface) at high μ^*. To enable a comprehensive comparative analysis, we also conducted simulations for clean bubbles and solid spheres, employing the same mesh configuration as outlined in § 2. However, we modified the dynamic boundary conditions at the interface, originally defined by (2.3b,c), to better represent the physical properties of clean bubbles and solid spheres. Specifically, the earlier conditions (2.3b,c)
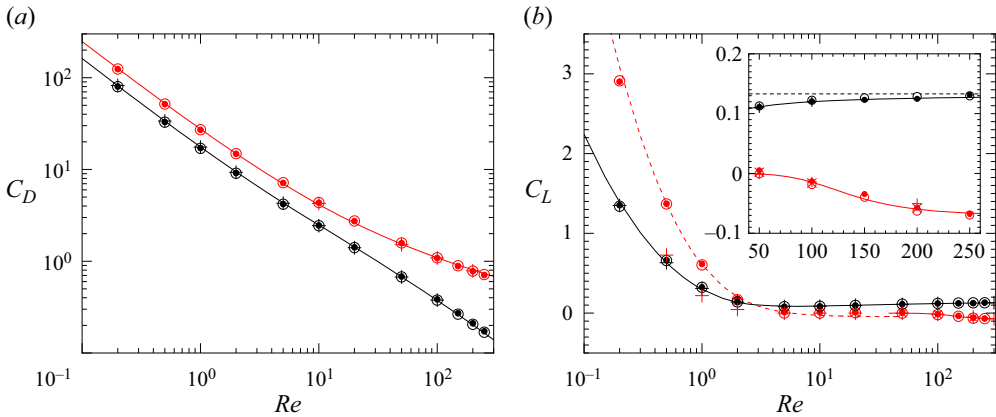
Figure 18. Results for C_D and C_L at $Sr = 0.2$ in the clean-bubble ($\mu^* \to 0$) and solid-sphere ($\mu^* \to \infty$) limits. ($\bigcirc$, red) and ($\bullet$, red), present simulation results for $\mu^* \to \infty$ and $\mu^* = 100$, respectively; $\bigcirc$ and $\bullet$, present simulation results for $\mu^* = 0$ and $\mu^* = 0.01$, respectively; ($+$, red) and ($\times$, red), data for solid spheres from Kurose & Komori (1999) and Bagchi & Balachandar (2002), respectively; $+$, data for clean bubbles from Legendre & Magnaudet (1998). red line and black line in panel (*a*), drag correlations from Schiller & Naumann (1933) and Mei *et al.* (1994), respectively; red line and red dashed line in panel (*b*), lift expression for solid spheres from Shi & Rzehak (2019, valid for $Re \geq 50$) and Candelier *et al.* (2023, valid for $Re \ll 1$), respectively; black line and black dashed line in panel (*b*), lift expression for clean bubbles from Legendre & Magnaudet (1998) and Auton (1987), respectively. All correlations used for predictions can be found in Appendix B.

were substituted with

$$
\begin{cases}
\boldsymbol{n} \times (\boldsymbol{\tau}^i \cdot \boldsymbol{n}) = \boldsymbol{n} \times (\boldsymbol{\tau}^e \cdot \boldsymbol{n}) = 0 & \text{for a clean bubble,} \\
\boldsymbol{n} \times \boldsymbol{u}^i = \boldsymbol{n} \times \boldsymbol{u}^e = 0 & \text{for a solid sphere.}
\end{cases}
\tag{A1}
$$

As shown in figure 18, the calculated hydrodynamic forces for $\mu^* = 0.01$ and $\mu^* = 100$ align well with those for a clean bubble and a solid sphere, respectively. Figure 18 also includes comparisons with drag and lift expressions as well as numerical data from prior research, focusing on clean bubbles or solid spheres, as detailed in the figure caption. Our results show very good agreement with these earlier studies, except for the C_L values at low Re. There, our results are consistent with the low-Re solution of Candelier *et al.* (2023) but are higher than the numerical data of Kurose & Komori (1999). This discrepancy is likely due to the smaller computational domain used in their simulations ($R_x^\infty = 20R$ compared with $100R$ in our study), which can lead to an underestimation of the lift force at low Re (Takagi & Matsumoto 1998).

In the second series of tests, we examined the dynamics at moderate viscosity ratios in a uniform flow, i.e. at $Sr = 0$. Assuming the flow to be axisymmetric, Rachih (2019, chapter 3.8) conducted a grid study up to $Re = 100$ using a similar numerical approach as implemented in this work. Their findings on flow structure and drag coefficients, derived from a grid of lower resolution than that in the present work, were closely aligned with earlier results from Oliver & Chung (1987) and Feng & Michaelides (2001), both of which also assumed an axisymmetric flow. Beyond $Re = 100$, several previous studies (Thorsen, Stordalen & Terjesen 1968; Edelmann *et al.* 2017; Rachih *et al.* 2020) have consistently reported a transition in the flow from axisymmetric to planar symmetric when the internal Reynolds number Re^i exceeds a critical value of approximately 300. To evaluate the ability of our numerical approach to replicate this transition, we focused on a scenario with
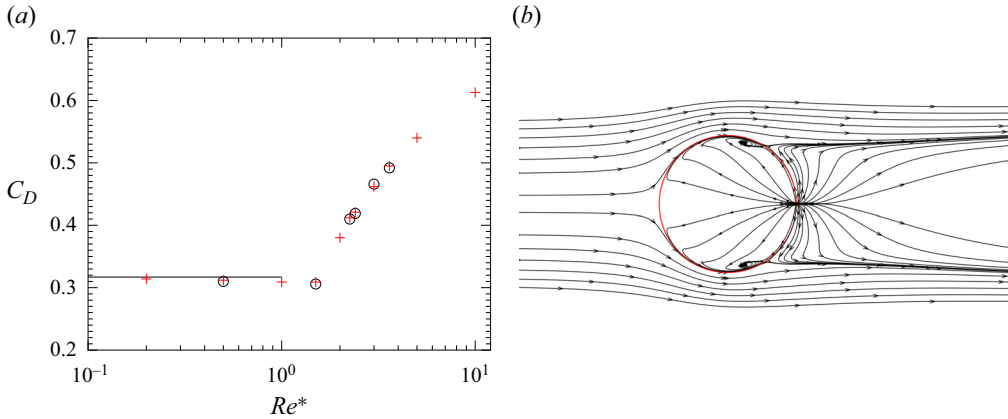
Figure 19. (a) C_D as a function of Re^* for $\mu^* = 0.5$, $Re = 200$ and $Sr = 0$. (b) Streamlines in the symmetry plane (red line represents the droplet surface) for $Re^* = 3$. In panel (a) +, red, our numerical results; $\bigcirc$, data from Edelmann *et al.* (2017); black line, the result from Feng & Michaelides (2001, $C_D = 0.317$), obtained under the assumption of axisymmetric flow.

$Re = 200$ and $\mu^* = 0.5$, varying Re^* from 0.2 to 10, which corresponds to an internal Reynolds number range of 40 to 2000.

The drag coefficients obtained from our simulations are presented in figure 19(a). They show good agreement with the previous fully 3-D simulation results from Edelmann *et al.* (2017). Specifically, our results indicate that the flow remains axisymmetric for $Re^* \leq 1.5$ (i.e. $Re^i \leq 300$), within which C_D exhibits only a weak dependency on Re^* (and consequently on ρ^*), closely aligning with the findings of Feng & Michaelides (2001). However, beyond $Re^i \approx 300$, we observe a pronounced flow separation inside the drop characterized by a distinct separation angle. Figure 19(b) shows the streamlines in the symmetry plane at $Re^* = 3$ (equivalent to $Re^i = 600$), where the internal flow detaches at the rear part of the droplet. The separation angle, measured from the rear stagnation point to the separation point, is approximately $54.7°$, closely matching the $55.5°$ value reported by Edelmann *et al.* (2017) under the same condition.

In the final series of tests, we focused on the drag and lift forces at $Re = 200$ and $Re^* = 5$ in a linear shear flow ($Sr = 0.2$), specifically at low-but-finite viscosity ratios $\mu^* = O(0.1)$. As highlighted in § 3.2 of the main paper, a notable characteristic in this regime is the increase in lift force following an internal bifurcation. To validate the reliability of this observation, we compared our numerical results with those from Zhang (2023, private communication), where the open-source code Basilisk (Popinet 2009, 2015) along with an innovative algorithm (Fang *et al.* 2021) for estimating the interfacial forces on non-body-fitted grids were employed. Figure 20 presents the time history of the drag and lift coefficients obtained at $\mu^* = 0.2$ (panel *a*) and $\mu^* = 0.5$ (panel *b*). Our results for both C_D and C_L show good agreement with those from Basilisk. Notably, both simulations indicate $C_L = Sr$ at $t = 0$ regardless of μ^*, consistent with the analytical solution derived by Legendre & Magnaudet (1998). Furthermore, C_L is observed to increase with time precisely when C_D reaches its peak value. The C_L values achieved in the quasi-steady state are found to be larger than the inviscid steady solution from Auton (1987), which predicts $C_L = 2Sr/3$. This excess is particularly evident in the case of $\mu^* = 0.5$.
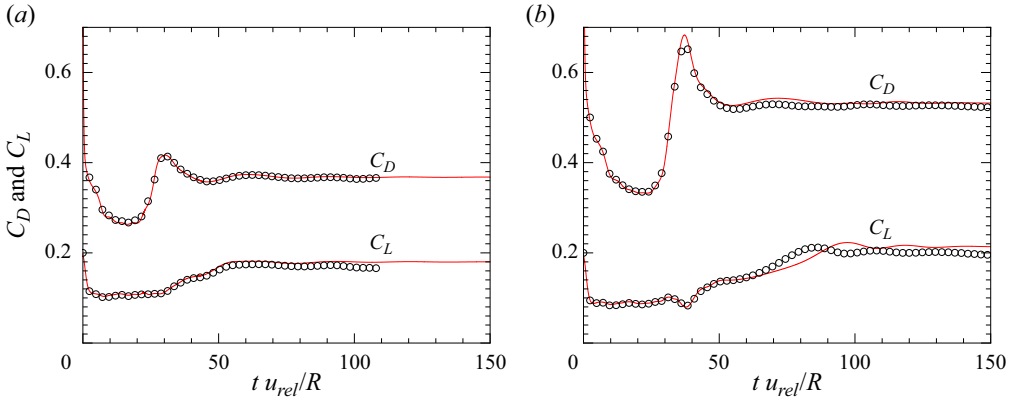
Figure 20. Time history of C_D and C_L for $Re = 200$, $Re^* = 5$ and $Sr = 0.2$. (a) $\mu^* = 0.2$; (b) $\mu^* = 0.5$. Red line, present numerical results; ◯, results from Zhang (2023, private communication) using Basilisk.

Appendix B. Correlations for C_D and C_L

We summarize in this section the available correlations for the drag and lift coefficients concerning clean bubbles (denoted by C_D^B and C_L^B) and solid spheres (denoted by C_D^S and C_L^S). In both cases, the ambient shear is known to cause an increase in drag (Legendre & Magnaudet 1998; Candelier *et al.* 2019). However, for $Sr \leq 0.2$, the relative magnitude of this shear-induced increase is small (Kurose & Komori 1999; Shi *et al.* 2020, 2021) and the drag coefficients in these two cases can be satisfactorily approximated using correlations for uniform-flow conditions (Schiller & Naumann 1933; Mei *et al.* 1994), namely

$$C_D^B = \frac{16}{Re}\left\{1 + \left[\frac{8}{Re} + \frac{1}{2}(1 + 3.315Re^{-1/2})\right]^{-1}\right\}, \tag{B1a}$$

$$C_D^S = \frac{24}{Re}(1 + 0.15Re^{0.687}). \tag{B1b}$$

These two expressions are valid throughout the range of Re considered in this work.

The lift coefficient for a clean bubble at arbitrary Re can be approximated using (Auton 1987; Legendre & Magnaudet 1997, 1998)

$$C_L^B = \{C_L^B(Re \ll 1)^2 + C_L^B[Re = O(100)]^2\}^{1/2}, \tag{B2a}$$

$$C_L^B(Re \ll 1) = \frac{8}{\pi^2}\frac{2.255\varepsilon}{(1 + 0.2\varepsilon^{-2})^{3/2}}, \tag{B2b}$$

$$C_L^B[Re = O(100)] = \frac{2}{3}Sr\frac{1 + 16Re^{-1}}{1 + 29Re^{-1}}, \tag{B2c}$$

where $\varepsilon = (Sr/Re)^{1/2}$ and the term $2Sr/3$ in (B4c) corresponds to the inviscid lift solution from Auton (1987).

For a solid sphere, the low-Re lift solution comprising the second-order inertial corrections (in terms of $(SrRe)^{1/2}$) reads (Saffman 1965; McLaughlin 1991; Legendre & Magnaudet 1998; Candelier *et al.* 2023)

$$C_L^S(Re \ll 1) = \frac{18}{\pi^2}\frac{2.255\varepsilon}{(1 + 0.2\varepsilon^{-2})^{3/2}} - 0.504Sr. \tag{B3}$$
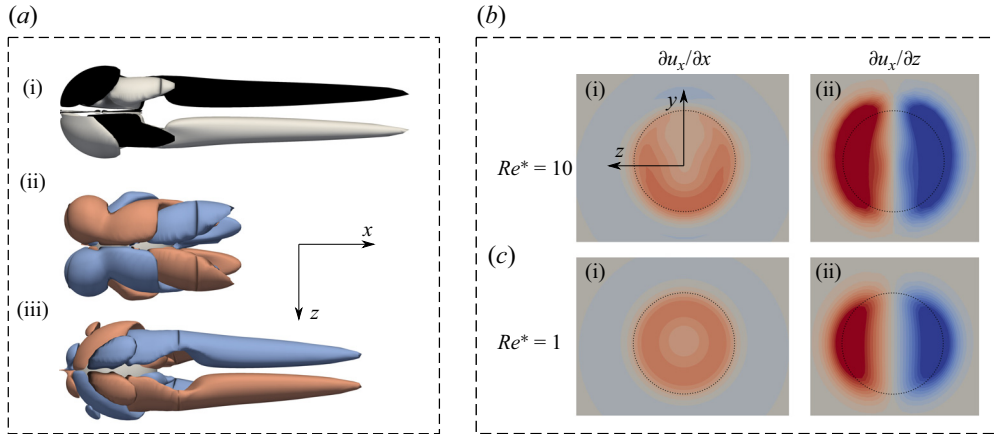
(a)   (b)

Figure 21. Flow structures at $\mu^* = 5$, $Re = 200$ and $Sr = 0.2$ for different internal Reynolds numbers. (*a*-i–*a*-iii) Isosurfaces of the streamwise vorticity ω_x, the combined source '$L + S$' in the budget equation (3.2) and the amplification term in (3.2) at $Re^i = 2000$. (*b*-i) and (*c*-i) (respectively, *b*-ii and *c*-ii) Extensional rate and spanwise gradient at $Re^i = 2000$ (respectively, $Re^i = 200$).

(In (B3), the second-order lift of $-0.504Sr$ was achieved by Candelier *et al.* (2023); its magnitude is approximately 2.7 times smaller than Saffman's incomplete prediction of $-11/8Sr$.)

The lift becomes vanishingly small for $Re = O(10)$ and changes its sign beyond $Re \approx 50$ (Kurose & Komori 1999; Bagchi & Balachandar 2002). For $50 \le Re \le 500$, its value can be approximated using (Shi & Rzehak 2019)

$$C_L^S(Re \gg 1) = -0.032 \exp(0.525Sr)\{1 + \tanh[5\log(ReSr^{0.08}/120)]\}. \tag{B4}$$

Appendix C. The negative lift at $(\mu^*, Re, Re^i) = (5, 200, 2000)$

The presence of a negative lift force at $(\mu^*, Re, Re^i) = (5, 200, 2000)$ (figure 5*b*) is somewhat unexpected. Our numerical results at lower Re^i suggested that: (i) the lift is only weakly affected by Re^i for viscosity ratios larger than approximately $\mu_c^* = 3$ and (ii) lift reversal occurs at a critical μ^* of approximately 10 (figure 15*a*). To unravel the mechanism behind the premature lift reversal at this high Re^i, we examined various flow structures for this condition, with key results summarized in figure 21.

Figure 21(*a*-i) illustrates the streamwise vorticity structure in the wake of the droplet. The orientations of the two streamwise vortices are opposite to their counterparts observed in the clean-bubble limit (figure 10*a*), in line with the negative lift force in this case. This suggests that the mechanism responsible for the lift generation in this case may still be understood by examining the various terms on the right-hand side of the budget equation (3.2). Figures 21(*b*-i) and 21(*c*-i) (and figures 21*b*-ii and 21*c*-ii) display the contour plots at the cross-stream plane $x = 2R$ of the two velocity gradients, $\partial u_x/\partial x$ and $\partial u_x/\partial z$, respectively, at $Re^i = 2000$ (and 200). The marked difference between results at the two Re^i, particularly the more pronounced $\partial u_x/\partial z$ at $Re^i = 2000$, confirms the onset of internal bifurcation at $(Re^i, \mu^*) = (2000, 5)$. Consequently, the threshold viscosity ratio $\mu_c^* = 3$ is only a reference value and loses its relevance at very high Re^i. Not surprisingly, both the combined source, '$L + S$', and the amplification term at $Re^i = 2000$ (figure 21*a*-ii,*a*-iii) are significantly more intense than those at $Re^i = 200$ (figure 14*a*-v,*b*-v). Specifically, at $Re^i = 2000$, the combined source downstream in the wake is predominantly positive for $z > 0$,

contrasting the corresponding case at $Re^i = 200$. This suggests that the internal bifurcation at high Re^i significantly enhances the 'S' mechanism, while primarily augmenting the 'L' mechanism for cases with $Re^i \leq 1000$. Given these insights, a comprehensive investigation into the shift in the primary enhanced mechanism at various Re^i is warranted. We plan to undertake this in future work, which will necessitate a much higher grid resolution to fully resolve the flow within the internal boundary layer.

Appendix D. Lift force inferred from the streamwise vorticity

It is well established that the lift force exerted on an object can be inferred from the vorticity field in the surrounding flow (Biesheuvel & Hagmeijer 2006; Hidman *et al.* 2022). In theory, once the vorticity distribution is experimentally or computationally ascertained, it becomes feasible to evaluate the lift force without necessitating knowledge of the pressure distribution at the body's surface. This profound theoretical concept is, however, of limited practical use in 3-D flows, primarily because the solution involves volume integrals. These integrals demand an accurate determination of the vorticity disturbance throughout the entire flow domain (Howe 1995; Magnaudet 2011). In this section, we revisit the simplified model originally proposed by de Vries *et al.* (2002) and later revised and used by Veldhuis (2007) and Zenit & Magnaudet (2009), which facilitates the estimation of lift force from the streamwise vorticity in the wake. We will demonstrate that, provided this vortical component is accurately known at a cross-stream plane sufficiently far downstream in the wake of the object, a qualitative estimation of the lift force is achievable.

To begin, we recall that the pair of streamwise vortices in the wake resemble two vortex tubes. Following the coordinates defined in the main body of the paper, these tubes are aligned in the x direction and symmetrically located with respect to the plane $z = 0$. Specifically, the tube in the half-space $z > 0$ rotates along e_ω^+, where e_ω^+ is either parallel or anti-parallel to e_x. Here, e_x denotes the streamwise direction, parallel to u_{rel}. In the inviscid limit, the induced velocity field of the two vortices generates a lift force acting on the bubble (Auton 1987; Biesheuvel & Hagmeijer 2006). The expression for this force is given by

$$F_L^\omega = -\rho_l z_c \Gamma u_{rel}(e_\omega^+ \cdot e_x)e_y, \tag{D1}$$

where Γ represents the circulation strength of each vortex tube and z_c is the separation between their centres.

For a viscous vortex, the vorticity is not compact but diffused around the vortex centre. Additionally, downstream in the wake, the circulation strength Γ may vary with the separation distance from the bubble due to viscous effects. The separation distance between the vortex centres also changes owing to vorticity diffusion. These features are highlighted in figure 22, which shows the structure of the streamwise vorticity at different distances downstream of a clean bubble for $Re = 200$ and $Sr = 0.2$. Clearly, the vorticity diffusion is not homogeneous and is significantly suppressed near the symmetry plane $z = 0$. Furthermore, the distance between the two vortices gradually increases with the separation from the bubble. Following Zenit & Magnaudet (2009), we estimate the circulation and the separation between the two vortices using

$$\Gamma = \left| \int_{\mathcal{C}} \boldsymbol{u} \cdot d\boldsymbol{r} \right| = \left| \int_{\mathcal{S}} \omega_x \, d\mathcal{S} \right|, \quad z_c \approx 2 \left| \frac{\int_{\mathcal{S}} \omega_x z \, d\mathcal{S}}{\int_{\mathcal{S}} \omega_x \, d\mathcal{S}} \right|, \tag{D2a,b}$$
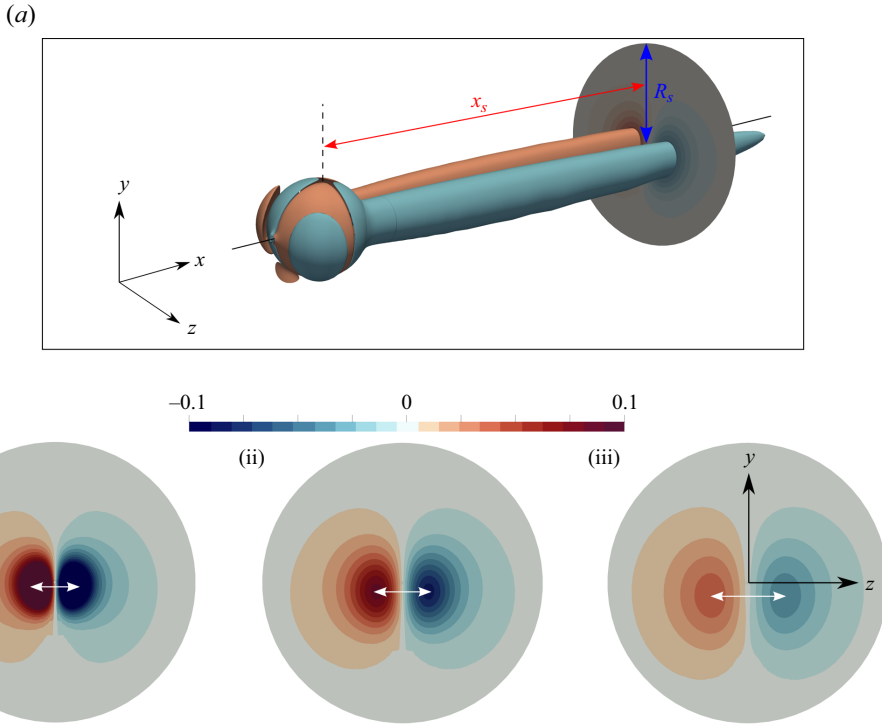
(a)

(b)

Figure 22. Structure of the normalized streamwise vorticity $(R/u_{rel})\omega_x$ in the cross-stream plane (illustrated in panel *a*) in the wake at varying distances downstream from a clean bubble at $Re = 200$ and $Sr = 0.2$. (*a*), Isosurfaces corresponding to $(R/u_{rel})\omega_x = \pm 0.05$. (*b*-i)–(*b*-iii) Isocontours of $(R/u_{rel})\omega_x$ in the cross-stream plane, which is a circular surface with a radius of R_S, centred at $(x = x_S, y = z = 0)$. Here, x_S takes values of $2R$, $5R$ and $10R$, respectively, the horizontal white arrowed line highlights the distance between the two points of maximum vorticity.

where $\mathcal{C}$ is a closed curve in the cross-stream plane enclosing one of the vortices and $\mathcal{S}$ is the area enclosed by $\mathcal{C}$. Note that, given the non-axisymmetric distribution of the vortex, the vortex centre is estimated from the centre of rotation of the velocity field (the point around which streamlines rotate), rather than from the point of maximum vorticity (Zenit & Magnaudet 2009).

To implement (D2*a,b*), we consider the cross-stream plane $\mathcal{S}$ as a half-circular surface with a radius of R_S, centred at $(x = x_S, y = z = 0)$, as illustrated in figure 22(*a*). To examine the model, we fix R_S at $10R$, a radial distance beyond which the disturbance induced by a sphere at $Re = O(100)$ is almost negligible (Magnaudet 2011), and analyse the flow past a clean bubble with $Re = 200$ at three different shear rates. The estimated Γ and z_c are depicted in figure 23(*a,b*) as functions of the normalized downstream distance x_S/R. As expected, both values exhibit a slight dependency on Sr in the near-wake region where $x_S \leq 5R$. In this region, where viscous effects are still pronounced, the orientation of the two vortex tubes is known to be slightly inclined downwards (Legendre & Magnaudet 1998; Shi *et al.* 2020), i.e. towards $-y$, the extent of which depends on Sr. This dependency, however, diminishes further downstream. Here, the normalized circulation (when divided by Sr) decreases with increasing separation distance from the bubble, whereas the reverse is true for z_c/R.

Figure 23(*c*) presents the estimated lift coefficients, denoted as C_L^{wake}, using (D1) and (D2*a,b*). The lift coefficients C_L, calculated by integrating the pressure and viscous
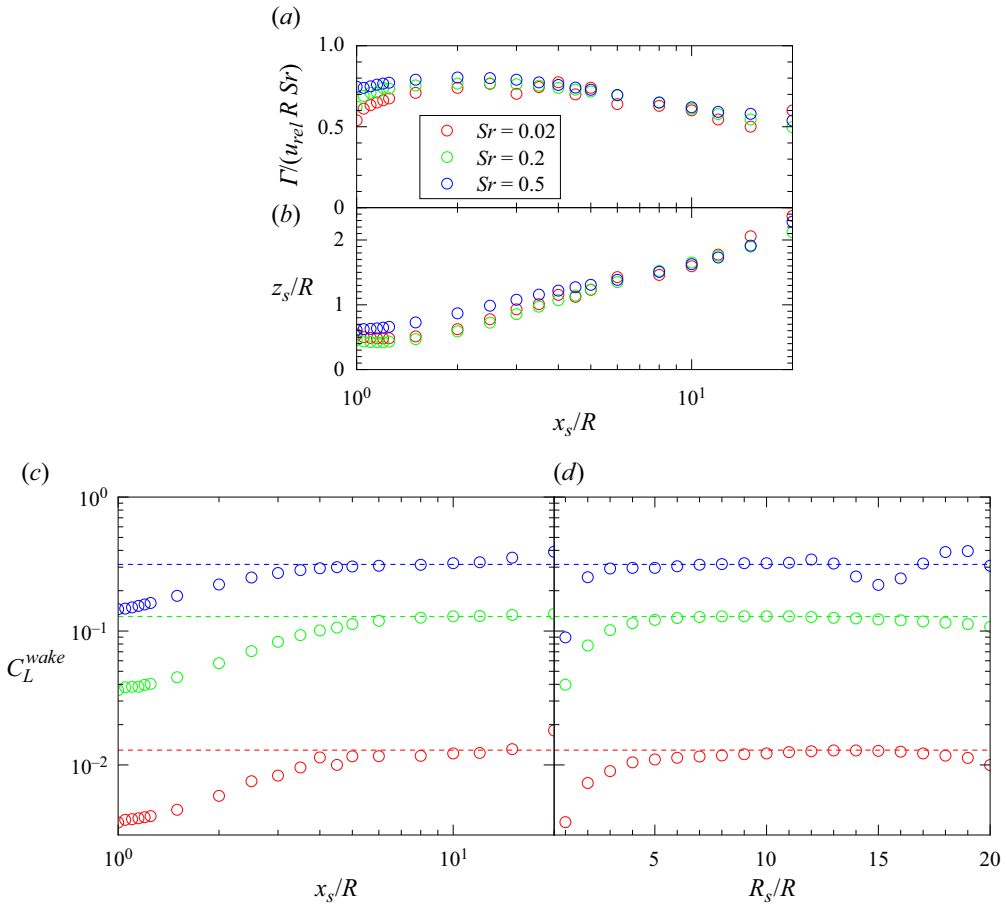
(*a*)

(*b*)

(*c*)   (*d*)

Figure 23. Results for (*a*) the circulation strength Γ, (*b*) separation distance z_c and (*c*,*d*) the vorticity-based lift coefficient C_L^{wake} of a clean bubble at $Re = 200$ with three different shear rates Sr. In panels (*a*–*c*), results are estimated at various distances downstream (denoted by x_S/R), and on the cross-stream plane $\mathcal{S}$, a half-circular surface centred along the line $y = z = 0$ with a fixed radius of $R_S = 10R$. In panel (*d*), results are estimated at a fixed distance downstream of $x_S/R = 10$, but considering different sizes of $\mathcal{S}$ (characterized by its radius R_S). In panels (*c*,*d*), the dashed lines represent the lift coefficient calculated by integrating the pressure and viscous stresses over the bubble interface, as described in (2.6*a*–*c*).

stresses over the bubble interface using (2.6*a*–*c*), are also presented (depicted as horizontal dashed lines). Irrespective of Sr, C_L^{wake} accounts for only approximately 30 % of C_L at $x = R$, but it gradually increases with increasing separation distance downstream. This increase saturates at $x_S \approx 5R$, beyond which C_L^{wake} closely aligns with C_L. For instance, the agreement between both is within 95 % at $x_S = 10R$. For $x_S \gtrsim 15R$, the vorticity becomes significantly diffused along the radial direction and the resolution of our numerical approach can no longer be assured. Consequently, the agreement starts to deteriorate in this extremely far-wake region.

The influence of the size of the cross-stream plane $\mathcal{S}$ on the estimated lift is examined by varying R_S, namely the radius of the cross-stream plane, from $1R$ to $20R$ while fixing x_S at $10R$. The corresponding C_L^{wake} as a function of R_S is shown in figure 23(*d*). Given the rapid decay (R_S^{-3}) of the disturbance in the far field (Magnaudet 2011), C_L^{wake} quickly converges to the reference value, C_L, at approximately $R_S = 5R$. A mismatch between the two values starts to occur at approximately $R_S = 15R$, owing to the insufficiency of grid

resolution, as previously mentioned. Based on these examinations, we set x_S and R_S both at $10R$ for estimating C_L^{wake}.

References

ADOUA, R., LEGENDRE, D. & MAGNAUDET, J. 2009 Reversal of the lift force on an oblate bubble in a weakly viscous linear shear flow. *J. Fluid Mech.* **628**, 23–41.

ALBERT, C., KROMER, J., ROBERTSON, A.M. & BOTHE, D. 2015 Dynamic behaviour of buoyant high viscosity droplets rising in a quiescent liquid. *J. Fluid Mech.* **778**, 485–533.

ASMOLOV, E.S. 1999 The inertial lift on a spherical particle in a plane Poiseuille flow at large channel Reynolds number. *J. Fluid Mech.* **381**, 63–87.

AUTON, T.R. 1987 The lift force on a spherical body in a rotational flow. *J. Fluid Mech.* **183**, 199–218.

BAGCHI, P. & BALACHANDAR, S. 2002 Effect of free rotation on the motion of a solid sphere in linear shear flow at moderate *Re*. *Phys. Fluids* **14**, 2719–2737.

BATCHELOR, G.K. 1967 *An Introduction to Fluid Dynamics*. Cambridge University Press.

BIESHEUVEL, A. & HAGMEIJER, R. 2006 On the force on a body moving in a fluid. *Fluid Dyn. Res.* **38**, 716.

BOTHE, D., SCHMIDTKE, M. & WARNECKE, H.J. 2006 Vof-simulation of the lift force for single bubbles in a simple shear flow. *Chem. Engng Technol.* **29**, 1048–1053.

BOUROUIBA, L. 2021 The fluid dynamics of disease transmission. *Annu. Rev. Fluid Mech.* **53**, 473–508.

BRETHERTON, F.P. 1962 The motion of rigid particles in a shear flow at low Reynolds number. *J. Fluid Mech.* **14**, 284–304.

CANDELIER, F., MEHADDI, R., MEHLIG, B. & MAGNAUDET, J. 2023 Second-order inertial forces and torques on a sphere in a viscous steady linear flow. *J. Fluid Mech.* **954**, A25.

CANDELIER, F., MEHLIG, B. & MAGNAUDET, J. 2019 Time-dependent lift and drag on a rigid body in a viscous steady linear flow. *J. Fluid Mech.* **864**, 554–595.

CITRO, V., TCHOUFAG, J., FABRE, D., GIANNETTI, F. & LUCHINI, P. 2016 Linear stability and weakly nonlinear analysis of the flow past rotating spheres. *J. Fluid Mech.* **807**, 62–86.

COLIN, C., FABRE, J. & KAMP, A. 2012 Turbulent bubbly flow in pipe under gravity and microgravity conditions. *J. Fluid Mech.* **711**, 469–515.

DANDY, D.S. & LEAL, L.G. 1989 Buoyancy-driven motion of a deformable drop through a quiescent liquid at intermediate Reynolds numbers. *J. Fluid Mech.* **208**, 161–192.

DI CARLO, D. 2009 Inertial microfluidics. *Lab on a Chip* **9**, 3038–3046.

DUINEVELD, P.C. 1995 The rise velocity and shape of bubbles in pure water at high Reynolds number. *J. Fluid Mech.* **292**, 325–332.

EDELMANN, C.A., LE CLERCQ, P.C. & NOLL, B. 2017 Numerical investigation of different modes of internal circulation in spherical drops: fluid dynamics and mass/heat transfer. *Intl J. Multiphase Flow* **95**, 54–70.

ELGHOBASHI, S. 2019 Direct numerical simulation of turbulent flows laden with droplets or bubbles. *Annu. Rev. Fluid Mech.* **51**, 217–244.

FABRE, D., TCHOUFAG, J. & MAGNAUDET, J. 2012 The steady oblique path of buoyancy-driven disks and spheres. *J. Fluid Mech.* **707**, 24–36.

FANG, Z., ZHANG, J., XIONG, Q., XU, F. & NI, M. 2021 Spatiotemporal evolutions of forces and vortices of flow past ellipsoidal bubbles: direct numerical simulation based on a cartesian grid scheme. *Phys. Fluids* **33**, 012108.

FENG, Z.G. & MICHAELIDES, E.E. 2001 Drag coefficients of viscous spheres at intermediate and high Reynolds numbers. *J. Fluids Engng* **123**, 841–849.

FUKUTA, M., TAKAGI, S. & MATSUMOTO, Y. 2008 Numerical study on the shear-induced lift force acting on a spherical bubble in aqueous surfactant solutions. *Phys. Fluids* **20**, 040704.

GODÉ, H. 2023 Flow and mass transfer prediction based on simulations around a spherical drop: from a local analysis to new models. PhD thesis, Toulouse, INPT.

GODÉ, H., CHARTON, S., CLIMENT, É. & LEGENDRE, D. 2023 Basset-boussinesq history force acting on a drop in an oscillatory flow. *Phys. Rev. Fluids* **8**, 073605.

HIDMAN, N., STRÖM, H., SASIC, S. & SARDINA, G. 2022 The lift force on deformable and freely moving bubbles in linear shear flows. *J. Fluid Mech.* **952**, A34.

HOWE, M.S. 1995 On the force and moment on a body in an incompressible fluid, with application to rigid bodies and bubbles at high and low Reynolds numbers. *Q. J. Mech. Appl. Maths* **48**, 401–426.

JOHNSON, T.A. & PATEL, V.C. 1999 Flow past a sphere up to a Reynolds number of 300. *J. Fluid Mech.* **378**, 19–70.

KUROSE, R. & KOMORI, S. 1999 Drag and lift forces on a rotating sphere in a linear shear flow. *J. Fluid Mech.* **384**, 183–206.

LEGENDRE, D. 2007 On the relation between the drag and the vorticity produced on a clean bubble. *Phys. Fluids* **19**, 018102.

LEGENDRE, D. 2024 Fluid dynamics of airtanker firefighting. *Annu. Rev. Fluid Mech.* **56**, 577–603.

LEGENDRE, D. & MAGNAUDET, J. 1997 A note on the lift force on a spherical bubble or drop in a low-Reynolds-number shear flow. *Phys. Fluids* **9**, 3572–3574.

LEGENDRE, D. & MAGNAUDET, J. 1998 The lift force on a spherical bubble in a viscous linear shear flow. *J. Fluid Mech.* **368**, 81–126.

LEGENDRE, D., RACHIH, A., SOUILLIEZ, C., CHARTON, S., & CLIMENT, É. 2019 Basset-boussinesq history force of a fluid sphere. *Phys. Rev. Fluids* **4**, 073603.

LIGHTHILL, M.J. 1956 Drift. *J. Fluid Mech.* **1**, 31–53.

LOHSE, D. 2022 Fundamental fluid dynamics challenges in inkjet printing. *Annu. Rev. Fluid Mech.* **54**, 349–382.

LOTH, E. 2008 Quasi-steady shape and drag of deformable bubbles and drops. *Intl J. Multiphase Flow* **34**, 523–546.

MAGNAUDET, J. 2003 Small inertial effects on a spherical bubble, drop or particle moving near a wall in a time-dependent linear flow. *J. Fluid Mech.* **485**, 115–142.

MAGNAUDET, J. 2011 A 'reciprocal' theorem for the prediction of loads on a body moving in an inhomogeneous flow at arbitrary Reynolds number. *J. Fluid Mech.* **689**, 564–604.

MAGNAUDET, J. & MOUGIN, G. 2007 Wake instability of a fixed spheroidal bubble. *J. Fluid Mech.* **572**, 311–337.

MAGNAUDET, J., RIVERO, M. & FABRE, J. 1995 Accelerated flows past a rigid sphere or a spherical bubble. Part 1. Steady straining flow. *J. Fluid Mech.* **284**, 97–135.

MAGNAUDET, J., TAKAGI, S. & LEGENDRE, D. 2003 Drag, deformation and lateral migration of a buoyant drop moving near a wall. *J. Fluid Mech.* **476**, 115–157.

MATAS, J.P., JEFFREY, F.M. & GUAZZELLI, E. 2009 Lateral force on a rigid sphere in large-inertia laminar pipe flow. *J. Fluid Mech.* **621**, 59–67.

MATHAI, V., LOHSE, D. & SUN, C. 2020 Bubbly and buoyant particle–laden turbulent flows. *Annu. Rev. Condens. Matter Phys.* **11**, 529–559.

MCLAUGHLIN, J.B. 1991 Inertial migration of a small sphere in linear shear flows. *J. Fluid Mech.* **224**, 261–274.

MEI, R., KLAUSNER, J.F. & LAWRENCE, C.J. 1994 A note on the history force on a spherical bubble at finite Reynolds number. *Phys. Fluids* **6**, 418–420.

MICHAELIDES, E.E. 2006 *Particles, Bubbles and Drops: Their Motion, Heat and Mass Transfer*. World Scientific.

OLIVER, D.L.R. & CHUNG, J.N. 1987 Flow about a fluid sphere at low to moderate Reynolds numbers. *J. Fluid Mech.* **177**, 1–18.

POPINET, S. 2009 An accurate adaptive solver for surface-tension-driven interfacial flows. *J. Comput. Phys.* **228**, 5838–5866.

POPINET, S. 2015 A quadtree-adaptive multigrid solver for the Serre–Green–Naghdi equations. *J. Comput. Phys.* **302**, 336–358.

RACHIH, A. 2019 Etude numérique du transfert de matière à travers l'interface d'une goutte sphérique en mouvement: mise en évidence des effets 3D. PhD thesis, Toulouse, INPT.

RACHIH, A., LEGENDRE, D., CLIMENT, É. & CHARTON, S. 2020 Numerical study of conjugate mass transfer from a spherical droplet at moderate Reynolds number. *Intl J. Heat Mass Transfer* **157**, 119958.

SAFFMAN, P.G. 1965 The lift on a small sphere in a slow shear flow. *J. Fluid Mech.* **22**, 385–400.

SCHILLER, L. & NAUMANN, A. 1933 Uber die grundlegenden berechnungen bei der schwerkraftaufbereitung. *Z. Verein. Deutsch. Ing.* **77**, 318–321.

SEGRÉ, G. & SILBERBERG, A. 1962*a* Behaviour of macroscopic rigid spheres in Poiseuille flow. Part 1. Determination of local concentration by statistical analysis of particle passages through crossed light beams. *J. Fluid Mech.* **14**, 115–135.

SEGRÉ, G. & SILBERBERG, A. 1962*b* Behaviour of macroscopic rigid spheres in Poiseuille flow. Part 2. Experimental results and interpretation. *J. Fluid Mech.* **14**, 136–157.

SHI, P. 2021 Hydrodynamic forces on a sphere translating steadily in a wall-bounded linear shear flow. PhD thesis, Technische Universität Dresden.

SHI, P. & RZEHAK, R. 2019 Lift forces on solid spherical particles in unbounded flows. *Chem. Engng Sci.* **208**, 115145.

SHI, P., RZEHAK, R., LUCAS, D. & MAGNAUDET, J. 2020 Hydrodynamic forces on a clean spherical bubble translating in a wall-bounded linear shear flow. *Phys. Rev. Fluids* **5**, 073601.

SHI, P., RZEHAK, R., LUCAS, D. & MAGNAUDET, J. 2021 Drag and lift forces on a rigid sphere immersed in a wall-bounded linear shear flow. *Phys. Rev. Fluids* **6**, 104309.

SUGIOKA, K.-I. & KOMORI, S. 2009 Drag and lift forces acting on a spherical gas bubble in homogeneous shear liquid flow. *J. Fluid Mech.* **629**, 173–193.

SUH, Y. & LEE, C. 2013 A numerical method for the calculation of drag and lift of a deformable droplet in shear flow. *J. Comput. Phys.* **241**, 35–57.

TAKAGI, S. & MATSUMOTO, Y. 1998 Numerical study on the forces acting on a bubble and particle. In *Proceedings of the 3rd International Conference on Multiphase Flow (ICMF'98), 8–12 June, Lyon, France*, p. 285.

TAKAGI, S. & MATSUMOTO, Y. 2011 Surfactant effects on bubble motion and bubbly flows. *Annu. Rev. Fluid Mech.* **43**, 615–636.

THORSEN, G, STORDALEN, R.M. & TERJESEN, S.G. 1968 On the terminal velocity of circulating and oscillating liquid drops. *Chem. Engng Sci.* **23**, 413–426.

TOMIYAMA, A., TAMAI, H., ZUN, I. & HOSOKAWA, S. 2002 Transverse migration of single bubbles in simple shear flows. *Chem. Engng Sci.* **57**, 1849–1858.

VELDHUIS, C.H.J. 2007 Leonardo's paradox: path and shape instabilities of particles and bubbles. PhD thesis, Univ. Twente.

DE VRIES, A.W.G., BIESHEUVEL, A. & VAN WIJNGAARDEN, L. 2002 Notes on the path and wake of a gas bubble rising in pure water. *Intl J. Multiphase Flow* **28**, 1823–1835.

ZENIT, R. & MAGNAUDET, J. 2009 Measurements of the streamwise vorticity in the wake of an oscillating bubble. *Intl J. Multiphase Flow* **35**, 195–203.

ZHANG, J. 2023 Private communication.